Pattern formation and transition to chaos in a chemotaxis model of acute inflammation *

Valeria Giunta†, Maria Carmela Lombardo‡, and Marco Sammartino§

Abstract. We investigate a reaction-diffusion-chemotaxis system that describes the immune response during an inflammatory attack. The model is a modification of the system proposed in Penner et al. [*SIAM Journal on Applied Dynamical Systems*, **11**, 2 (2012), pp. 629-660]. We introduce a logistic term in the immune cell dynamics to reproduce the macrophages' activation, allowing us to describe the disease evolution from the early stages to the acute phase. We focus on the appearance of pattern solutions and their stability. We discover steady-state (Turing) and Hopf instabilities and classify the bifurcations deriving the corresponding amplitude equations. We study stationary radially symmetric solutions and show that they reproduce various inflammatory aggregates observed in the clinical practice. Moreover, the model supports oscillating-in-time spatial patterns, thus giving a theoretical explanation of the periodic appearance of inflammatory eruptions typical of *Recurrent Erythema Multiforme*. A detailed numerical bifurcation analysis indicates that the inclusion of the logistic growth term is crucial for the occurrence of a sequence of bifurcations leading to spatio-temporal chaos. In the parameter space, there are large regions where the model system displays critical behavior.

Key words. Inflammation model, Chemotaxis, Pattern formation, Bifurcation analysis, Transition to chaos, Criticality

AMS subject classifications. 92C15, 92C17, 35B36, 35B32, 65P20

1. Introduction.

In this paper, we shall introduce a reaction-diffusion-chemotaxis model that describes the initial stages of inflammatory disease. Using the normal form analysis we shall construct solutions representing coherent aggregates of inflammation and oscillatory patterns. To the best of our knowledge, the model is the first to reproduce the formation and the dynamics of localized patches of skin rashes, typically observed in the clinical practice.

1.1. The physiological basis of inflammation.

Inflammation is the body response to outside threats like stress, infection, pathogens, or damaged cells. It is a highly complex process, where pro- and anti-inflammatory agents work synergistically to ensure a quick restoration of tissue health [85]. A dis-regulation of the inflammatory response can give rise to chronic inflammation [46] and lead to a wide range of diseases, such as cancer [67], atherosclerosis [22], asthma [32] and autoimmune diseases [23].

There is a consensus that the macrophages are the immune system cells that play a pivotal role in all stages of the inflammation [9, 20]. In the presence of a threat, macrophages enter an activated state that may display two different phenotypes [53]: in the early stages of inflam-

*Submitted to the editors August 2020.

Funding: The authors acknowledge the financial support of GNFM-INdAM and the Italian MIUR through project PRIN2017 *Multiscale phenomena in Continuum Mechanics: singular limits, off-equilibrium and transitions* (project no. 2017YBKNCE)

†School of Mathematics and Statistics, University of Sheffield, UK (v.giunta@sheffield.ac.uk).

‡Department of Mathematics, University of Palermo, Italy (mariacarmela.lombardo@unipa.it).

§Department of Engineering, University of Palermo, Italy (marco.sammartino@unipa.it).

mation, they mainly present the M1(classically activated) phenotype [15], characterized by pro-inflammatory activity: they release toxicants for eliminating the threat and produce pro-inflammatory mediators (cytokines) that significantly contribute to the recruitment and the activation of more immune cells [42, 44] . Subsequently, macrophages change their polarization into the M2 [52, 81] (alternatively activated) state, aimed at suppressing the inflammatory activity by releasing pro-resolution mediators (such as IL-10), which inhibit the production of pro-inflammatory cytokines [82].

The cytokines IFN-γ, IFN-α, TNF-α are involved in the activation of macrophages [9, 82]. On the opposite side, IL-10 and IL-11, among others, have a strong anti-inflammatory effect and reduce the production of pro-inflammatory mediators from activated macrophages [1]. Finally, the so-called chemokines stimulate chemotaxis [42, 82], namely the directed movement of cells along a concentration gradient of a chemical.

In the present paper, following [66], we shall denote by chemokines the pro-inflammatory mediators, also responsible for chemotaxis, and by cytokines the anti-inflammatory molecules.

1.2. Modeling and mathematical aspects of reaction-diffusion-chemotaxis systems.

In the last years, to explain the evolution of the inflammatory process, several mathematical modeling approaches have emerged, The models, mainly based on ordinary differential equations systems, have played an essential role in understanding the dynamical relationship between the many pathological mechanisms involved in inflammation [20, 62, 69, 87, 89, 90]. However, due to the extreme complexity of the inflammatory signaling pathways, only a few of them have taken into account the species' spatial distribution. The first study on rash formation based on reaction-diffusion systems is in [38], where the authors selected simple toy model equations (Segel and Levin model and Keener and Tyson model) to represent the primary mechanisms for the autogenic formation of Type I (stationary) and Type II (moving waves) patterns. In the same spirit, and seeking to understand the genesis of self-supporting inflammatory traveling waves in the absence of specific pathogenic stimuli, a three-species reaction-diffusion-chemotaxis system was proposed and studied in [66]. It describes the interaction between a fixed population of immune cells, a pro-inflammatory chemokine, and an anti-inflammatory cytokine. The reaction term does not consider the cell kinetics; this implies that during the evolution of the inflammatory response, the number of activated macrophages remains constant. Under these assumptions, the authors analyzed stationary and traveling-wave solutions; they showed that the inclusion of inhibition of chemoattractant production by the anti-inflammatory chemical determines oscillatory instabilities corresponding to propagating patterns.

In this paper, to describe macrophages recruitment during the inflammatory response, we generalize the model presented in [66] introducing a logistic term in the macrophages equation. There is, in fact, experimental evidence that, after the tissue-resident macrophages have initiated the inflammatory cascade, activation of the immune cells persists with the goal to amplify the inflammatory response [42]. After initial recognition of the microbial challenge, resident macrophages, also favored by the pro-inflammatory activity performed by the chemokines [53], drive the influx of monocyte-derived macrophages as a source of further inflammation [17].

Therefore, including in the model the activation term allows us to describe the early

stages of the inflammatory response, namely, the cascade of both pro-inflammatory and anti-inflammatory species following the initial insult and their corresponding spatial dynamics. Moreover, it yields the possibility of investigating the effect of varying the strength of the activation rate on the system dynamics: since identification and regulation of the activation status of macrophages is believed to be a useful diagnostic and therapeutic tool for various diseases [72], such analysis can provide valuable information about the effects of aberrant or impaired activation on inflammation and the effect of different therapeutic strategies.

The cells' movement is modeled through a linear diffusive term, which accounts for random motion, and through a nonlinear chemotactic term, which describes cell motility along the chemical gradient. The chemotactic term is of the widely used Keller-Segel-type that incorporates a signal-dependent sensitivity function [34]: it reproduces the fact that, at high concentrations of the chemical, the cell receptors are all occupied so that the macrophages do not sense the gradient.

Loss of regularity is a well known and intensively studied phenomenon displayed by the solutions of the classical Keller-Segel system with linear sensitivity function; for example, on 2-dimensional spatial domains, the explosion in a finite time may occur if the initial mass is above a critical threshold [36, 96]. Instead, the inclusion of a limited-growth chemotactic term [2, 19, 91] or of a logistic-type reaction term [34, 61, 62, 95] has blow-up-inhibiting effects. Therefore, the saturating functional form of the chemoattractant's sensing, other than being a biologically meaningful hypothesis, is sufficient to avoid blow-up of the solutions. Moreover, the presence of the quadratic absorption term in the logistic source, accounting for competition-induced mechanisms that are generally present in most situations of biological importance, also prevents the non-physical unboundedness of solutions. The realistic combination of limited chemotaxis and growth yields a class of well-posed models of increased complexity whose solutions display a rich structure of asymptotic profiles and dynamics [21, 41, 50, 51, 64].

In what follows we shall keep the mathematical description of a yet complicated phenomenon simple: the focus of this work is to show that a simplified model, which includes the basic mechanisms of activation and chemotactic movement, can reproduce some pathologically relevant clinical features and, possibly, account for the evolution of idiopathic diseases.

1.3. Results. We shall first investigate the conditions on the system parameters that determine the excitation of Turing and wave instabilities. We stress that in the set-up of the model, we shall consider only mechanisms whose role is acknowledged in the medical literature and whose corresponding functional forms have been experimentally verified. Therefore all numerical values of the parameters used in this paper will be taken from the experimental literature, except for the macrophages activation rate whose value has been estimated in [70]. We shall show that if the chemotactic coefficient is small, namely below the thresholds for both the Turing and wave instabilities to set in, then the aggregation strength is not sufficient to induce the formation of highly localized zones of inflammation. In this case, the model reproduces a diffused inflammatory state of the type observed in many cutaneous rashes.

On the other hand, high values of the chemotaxis can induce two different instabilities, depending on the value of the parameter that regulates the anti-inflammatory time-scale: if the anti-inflammatory response is fast, a large chemotactic term can excite a Turing instability with the consequent formation of stationary patterns. In this case, the investigation of the

system dynamics on 2D spatial domains will show that the model provides the key mechanism for the formation of the skin rashes observed in Erythema Annulare Centrifugum (EAC), a very aggressive form of cutaneous rash [16, 78], characterized by symmetrically distributed target lesions with typical ring-shaped patterns [39].

For large values of both the anti-inflammatory time scale and the chemotaxis coefficient, the linear analysis predicts the presence of large regions in the parameters space where wave instability occurs. The corresponding numerical simulations show the formation of oscillating-in-time spatial patterns, that qualitatively reproduce the time-periodic appearance of localized skin eruptions characteristic of the Recurrent Erythema Multiforme (REM) [48, 75, 93]. Therefore the present model proposes a possible mechanism for explaining the insurgence of recurrent inflammations, whose etiology is still unknown.

A significant consequence of the introduction of cellular growth is the occurrence of spatio-temporal irregular solutions, that one cannot observe in the absence of the cell kinetic term. We shall show that when macrophages' activation rate is absent, the Turing patterns are metastable: on a logarithmic time scale, they display coarsening dynamics, whereas the creation of new structures is ruled out. Instead, increasing the macrophages activation rate, we shall observe the occurrence of a sequence of successive bifurcations, leading to chaotic spatio-temporal dynamics characterized by irregularly merging and emerging structures. The presence of aperiodic merging-emerging phenomena has also been detected in Keller-Segel-type models with logistic growth term [21, 50, 64].

As a final remark, we mention the derivation in Subsection 3.1 of the necessary and sufficient conditions for the onset of instability in a three-component reaction-diffusion-chemotaxis system. When the diffusion matrix is diagonal and semidefinite positive, one can find several theorems stating the conditions for the linear instability of a multi-component system [3, 14, 33, 73]. Less attention has been paid to instability in chemotaxis models: in these cases, commonly, one invokes the Routh-Hurwitz or the Gershgorin Circle Theorem, both asserting only sufficient conditions to localize the corresponding linearized problem's eigenvalues. In the present paper, we shall address the root's localization problem through the Sylvester criterion, namely studying the positive definiteness of the Bezoutiant matrix [68], obtaining necessary and sufficient conditions for the onset of instability. We believe that this approach can be useful in the analysis of analogous models.

1.4. Plan of the paper. In Section 2, we shall illustrate the main assumptions underlying the construction of the model and present the ranges of numerical values of the parameters used in the simulations. In Section 3, we shall perform the linear stability analysis to determine the conditions on the system parameters for the occurrence of Turing and wave instability. In Section 4, through a weakly nonlinear analysis, we shall derive the amplitude equation of the stationary patterns to characterize supercritical and subcritical transitions at the onset. In Section 5, we shall investigate the role of different activation rates on the system dynamics: we shall show that the inclusion of the growth term induces a sequence of successive oscillatory bifurcations leading to chaotic dynamics. In Section 6, we shall investigate radially symmetric solutions and prove that the proposed model can reproduce the formation of qualitatively different ring-shaped skin eruptions observed in EAC. In Section 7, we support the analysis of Section 6 through extensive numerical simulations performed on fully 2D domains. Finally,

for the reader's convenience, we have added some supplementary material where we report the proofs of the Theorems and some technical details.

2. A mathematical model of inflammation. In this Section we shall present a chemotaxis-reaction-diffusion model that describes the interaction between a population of macrophages $m(\mathbf{x},t)$, a pro-inflammatory chemokine $c(\mathbf{x},t)$, and an anti-inflammatory cytokine $a(\mathbf{x},t)$. All the quantities are intended as concentrations in space.

The proposed model generalizes the system introduced by [66] in the sense that it takes into account cell kinetics.

2.1. Activated macrophages. We assume that the following equation rules the evolution of the immune cells population:

$$\frac{\partial m}{\partial t} = \underbrace{\nabla_x \cdot (D_m \nabla_x m)}_{\text{Diffusion}} - \underbrace{\nabla_x \cdot \left(\psi \frac{m}{(1+\alpha c)^2} \nabla_x c \right)}_{Chemotaxis} + \underbrace{rmc\left(1 - \frac{m}{\bar{m}}\right)}_{Activation}, \tag{2.1}$$

The first term in Equation (2.1) describes the diffusion of the cells due to random motion; D_m is the diffusivity coefficient. The second term models the chemoattraction of macrophages along the gradient of the chemical signal. The sensitivity function $\bar{\chi}(c) = \frac{\psi}{(1+\alpha c)^2}$ that describes the rate of attraction, has been derived in the so-called *receptor-binding* model [34] and displays saturation for increasing values of c. The parameter ψ represents the maximal chemotactic rate; α modulates the saturation of the chemokine receptors. The third term in (2.1) is the novelty of the present model with respect to the dynamics presented in [66], where the number of activated immune cells, imposed by the initial condition, was held fixed after activation. Here we want to consider the effects of macrophages activation driven by inflammation, which might concur to the settling of a recurrent or persistent inflammatory state. In fact, it is well known that, due to the presence of pro-inflammatory chemical species, macrophages release toxicants agents, such as oxygen-free radicals [85]. Such toxicants, if on the one hand, can kill bacteria and destroy foreign bodies; on the other hand, they can also damage hosting tissue, inducing more inflammation [40] with the consequent recruitment of more immune cells. Hence, cytokines and macrophages act to amplify the inflammatory signal, promoting the activation of more immune cells [53]. Therefore, we introduce an activation term with mass-action type kinetics, proportional to the product of the macrophage and chemokine densities, and that saturates for the increasing concentration of the macrophages to mimic cell depletion. The same functional form was adopted in [43]. Here r and $\bar{m}$ represent the growth rate coefficient and the carrying capacity of the activated macrophages, respectively. The carrying capacity $\bar{m}$ has the meaning of the average density of the resting macrophages; the resting macrophages act as a cellular pool for the activated macrophages, so that, when $m = \bar{m}$, all the resting immune cells have turned into their active state. As in [66], the initial insult that triggers the immune system is described by the initial conditions, assuming that the pathogen has already been eliminated, as typical in runaway inflammations.

2.2. Pro- and Anti-Inflammatory Molecules. We assume that the pro- and anti-inflammatory cytokines have the same evolution, namely:

$$\begin{aligned}\frac{\partial c}{\partial t} &= \underbrace{\nabla_x \cdot (D_c \nabla_x c)}_{\text{Diffusion}} + \underbrace{\nu_c \frac{m}{1+\beta a^\rho}}_{\text{Production}} - \underbrace{\mu_c c}_{\text{Decay}},\\ \frac{\partial a}{\partial t} &= \underbrace{\nabla_x \cdot (D_a \nabla_x a)}_{\text{Diffusion}} + \underbrace{\nu_a \frac{m}{1+\beta a^\rho}}_{\text{Production}} - \underbrace{\mu_a a}_{\text{Decay}}.\end{aligned} \tag{2.2}$$

The first term on the right-hand side of both equations represents the diffusion of molecules with diffusivity coefficients D_c and D_a, respectively. The second term in (2.2) describes the production of the chemical species by macrophages, the denominator representing the inhibitory effect of the anti-inflammatory cytokines on the activity of previously activated macrophages [1]. The parameters ν_c and ν_a are the production rates per macrophage, while β and ρ control the inhibitory effects of the cytokines. Finally, the last terms in (2.2) represent the natural decay of both molecules, with decay rates μ_c and μ_a, respectively.

Since the production of anti-inflammatory mediators is relatively late compared to the production of pro-inflammatory chemicals, following [66], we shall set $D_a = D_c/\tau$, $\nu_a = \nu_c/\tau$ and $\mu_a = \mu_c/\tau$, where τ is a small parameter which regulates the slower time scale of the anti-inflammatory molecules.

2.3. The non-dimensional form of the model. We introduce the following set of non-dimensional variables and parameters

$$\begin{aligned} m^* = \frac{m}{\bar{m}},\ c^* = \frac{\mu_c}{\nu_c \bar{m}} c,\ a^* = \frac{\mu_a}{\nu_a \bar{m}} a,\ D^* = \frac{D_m}{D_c},\ t^* = \mu_c t,\\ x^* = \sqrt{\frac{\mu_c}{D_c}}\, x,\ r^* = \frac{\bar{m}\nu_c}{\mu_c^2} r,\ \chi = \frac{\psi \nu_c \bar{m}}{\mu_c D_c},\ \alpha^* = \frac{\nu_c \bar{m}}{\mu_c}\alpha,\ \beta^* = \frac{\nu_a \bar{m}}{\mu_a}\beta. \end{aligned} \tag{2.3}$$

With this non-dimensionalization, we have chosen chemokines' average lifetime as the reference time scale and the average distance traveled by a pro-inflammatory molecule during its average lifetime as the reference spatial-scale.

Using (2.3), the model can be written in the following non-dimensional form, where we have dropped the asterisks:

$$\begin{aligned} \frac{\partial m}{\partial t} &= D\Delta m - \nabla \cdot \left(\chi \frac{m}{(1+\alpha c)^2} \nabla c \right) + rmc(1-m),\\ \frac{\partial c}{\partial t} &= \Delta c + \frac{m}{1+\beta a^\rho} - c,\\ \frac{\partial a}{\partial t} &= \frac{\Delta a}{\tau} + \frac{1}{\tau}\left(\frac{m}{1+\beta a^\rho} - a \right). \end{aligned} \tag{2.4}$$

When $r = 0$, system (2.4) reduces to the model reported in [66].

If our system evolves on the spatial domain Ω, at the boundary we impose homogeneous no-flux Neumann boundary conditions that reduce to:

$$\nabla m = \nabla c = \nabla a = 0, \quad \text{on} \quad \partial\Omega. \tag{2.5}$$

2.4. Parameter estimation. In this section, we give an estimation of the parameters appearing in the system (2.1)-(2.2). The assessment of precise numerical values to the different constants is highly arduous, not only because of the experimental difficulties associated with the measurements but also because such values significantly depend on the tissue where inflammation occurs. For these reasons, we have usually given a range of values for the parameters, taking into account both available experimental data and estimates derived in mathematical models of inflammation already presented in the literature.

We shall use the following units: min for the time, μm for the length, nM for the chemical concentration and μm^{-3} for the density of cells.

The diffusion coefficients, both for macrophages and signaling molecules, are easily found in the literature. The chemokine diffusion rate, is usually estimated using the molecular weight [31], and we adopt the value given by [49], that is $D_c = 900\ \frac{\mu\text{m}^2}{\text{min}}$. Concerning the macrophage diffusion rate, there is no general consensus on its value because there is a strong dependence on the tissue and on other biological factors involved, among which there is also chemokine concentration. In the paper [49], the range of values $[240; 4200]\ \mu\text{m}^2/\text{min}$ is reported. Notice also that, since chemokines are smaller than immune cells, they can move relatively faster and, in the huge range of variability reported in [49] (the range given in [30] is even wider), it is reasonable to assume that the macrophage diffusion rate is lower than the signaling molecules' diffusivity, i.e., $D_m < D_c$. Therefore, we fix the value of D_m in the lower end of the range reported in [49], and we pick $D_m = 800\ \frac{\mu\text{m}^2}{\text{min}}$; we leave to future work an exploration of the effect of varying the parameter D_m, also taking into account a possible dependence on c.

The functional dependence of the chemotactic function $\bar{\chi}(c) = \frac{\psi}{(1+\alpha c)^2}$ was experimentally verified by [24], where nevertheless no estimate of the coefficient ψ was given. We have therefore estimated a range of values for this parameter using the experimental data presented by [84], where the following expression of the chemotactic function was used:

$$\frac{\chi_0 N_{T_0} K_d\, f\, S}{(K_d + c)^2}.$$

In the above expression, the experimentally measured value of $\chi_0 N_{T_0}$ is 0.2 cm, K_d is the receptor equilibrium dissociation constant and the values of f and S have been measured for values of the chemoattractant concentration ranging from 0 to 3×10^{-7} M: namely, the authors reported the values of $S \in [4.3; 30]\,\mu\text{m/min}$, and $f \in [0.2, 1]$.

In their experiments, the authors used a chemoattractant (the FNLLP) whose value of the equilibrium dissociation constant K_d (2×10^{-8} M) lies within the interval measured for the the dissociation constants of the chemokines involved in the inflammatory processes [5, 77].

Recalling that $\text{nM} = 10^{-9}$ Mwt pg μm^{-3}, where Mwt is the molecular weight of the cytokines expressed in kDa (we used the value of 17 kDa for the molecular weight of IL-1β), we have obtained $\alpha = 3 \times 10^6 \frac{\mu\text{m}^3}{\text{pg}}$. From $\psi = \chi_0 N_{T_0} f\, S/K_d$, we have finally estimated $\psi \in [5 \times 10^9;\ 176 \times 10^9]\ \frac{\mu\text{m}^5}{\text{min pg}}$.

We have adopted the numerical value of r given by [70], $r = 1.7 \times 10^5\ \frac{\mu\text{m}^3}{\text{pg min}}$; this value also falls within the range reported in [94].

The numerical values of the density of resting macrophages $\bar{m}$ can vary significantly from tissue to tissue. Moreover the experimental estimate of $\bar{m}$ is made more difficult from the fact

that it is problematic to distinguish between different macrophage subpopulations (resident, classically and alternatively activated), see [12]. The values reported in the medical literature go between 10^{-6}cells/μm^3 [59] and 10^{-4}cells/μm^3 [45]. In dermis, from the reference [92], one can estimate that $\bar{m} = 5 \cdot 10^{-5}$cells/$\mu m^3$; in [83], the range $[10^{-5}; 6 \cdot 10^{-5}]$cells/$\mu m^3$ is reported. In this paper we fix $\bar{m} = 3 \cdot 10^{-5}]$cells/$\mu m^3$.

The chemokine production rate per macrophage, ν_c, was experimentally measured in vitro by [47, 57] and, based on these results, we have adopted the interval $(5.7 \times 10^{-6} - 1.96 \times 10^{-5})$ pg min^{-1} cells^{-1}.

To estimate the inhibitor rate β and the parameter ρ introduced in the chemokine production term, we followed [87], where the inhibitory effect of the anti-inflammatory chemical was reproduced by the functional form $\frac{K_a}{K_a+a}$, where K_a is the dissociation constant of the cytokine a, from which $\beta = 1/K_a$ and ρ=1.

The range for chemokine decay $\mu_c \in [0.001;\ 0.03]$ min^{-1} is taken from [57].

Finally, recalling that τ controls the slow time scale of the cytokine dynamics and that the anti-inflammatory mediators are detected in the site of inflammation within few minutes to five days after the injury [18], we set $\tau \in [1; 7200]$.

In Table 1 we report the ranges of values for every parameter appearing in eqs.(2.1)-(2.2), and in Table 2 we report the corresponding ranges of the dimensionless parameter values used in the numerical simulations.

Table 1: Values of the parameters appearing in equations (2.1)-(2.2) and used in the present paper. For a discussion see the text.

Parameter	Description	Value	Source
D_m	Macrophages random motility	800 $\frac{\mu m^2}{min}$	[84]
D_c	Chemokine random motility	900 $\frac{\mu m^2}{min}$	[49]
ψ	Chemoattraction	$[5 \times 10^9;\ 176 \times 10^9]$ $\frac{\mu m^5}{min\ pg}$	[84]
α	Receptor-binding constant	3×10^6 $\frac{\mu m^3}{pg}$	[84]
r	Macrophages activation rate	1.7×10^5 $\frac{\mu m^3}{pg\ min}$	[70]
$\bar{m}$	Average resident macrophages density	3×10^{-5} $\frac{cells}{\mu m^3}$	[83, 92]
ν_c	Chemokine production rate	$[5.7 \times 10^{-6};\ 1.96 \times 10^{-5}]$ $\frac{pg}{min\ cells}$	[47, 57],
β	Inhibition rate	3×10^6 $\frac{\mu m^3}{pg}$	Estimated
ρ	Inhibition rate	1	[87]
μ_c	Chemokine decay rate	$[0.001;\ 0.03]$ min^{-1}	[57]

Table 2: Values of the dimensionless parameters appearing in equations (2.4) and used in this paper.

Parameter	Description	Value
D	Macrophages random motility	0.9
χ	Chemoattraction	$[3.17 \times 10^{-2};\ 115]$
α	Receptor-binding constant	$[0.017;\ 1.76]$
β	Inhibition rate	$[0.017;\ 1.76]$
ρ	Inhibition exponent	1
r	Macrophages activation rate	$[0.03;\ 100]$
τ	slow time scale	$[1;\ 7200]$

3. Linear Analysis. The non-dimensional model has a unique nontrivial homogeneous steady state $P^* = (m^*, c^*, a^*) = (1, a_0, a_0)$, where $a_0 = \frac{-1+\sqrt{1+4\beta}}{2\beta} > 0$ for all $\beta > 0$. It corresponds to a biological state of spatially uniform inflammation where all the resident macrophages are activated and the immune response is sustained by a non-zero value of the pro-inflammatory and anti-inflammatory chemicals.

The linearization of system (2.4) in the neighborhood of the equilibrium point P^* gives:

$$\frac{\partial}{\partial t}\begin{bmatrix} m \\ c \\ a \end{bmatrix} = \begin{bmatrix} D & -\frac{\chi}{(1+\alpha a_0)^2} & 0 \\ 0 & 1 & 0 \\ 0 & 0 & \frac{1}{\tau} \end{bmatrix} \Delta \begin{bmatrix} m \\ c \\ a \end{bmatrix} + \begin{bmatrix} -ra_0 & 0 & 0 \\ \frac{1}{1+\beta a_0} & -1 & -\frac{\beta}{(1+\beta a_0)^2} \\ \frac{1}{(1+\beta a_0)\tau} & 0 & -\left(\frac{\beta}{(1+\beta a_0)^2\tau} + \frac{1}{\tau}\right) \end{bmatrix}$$

$$\equiv \mathcal{D}\Delta[m, c, a]^T + \mathcal{K} \tag{3.1}$$

where $\mathcal{D}$ is the linearized diffusion matrix and $\mathcal{K}$ is the linearized kinetics.

We now suppose that the spatial domain $\Omega = [0, 2\pi]$, and look for solutions of the form $(m, c, a) = (\hat{m}, \hat{c}, \hat{a})e^{\lambda t}\Phi_k(x)$, where $\Phi_k(x) = \cos(kx)$ are the eigenfunctions of Δ operator with Neumann boundary conditions. We obtain the following eigenvalue problem:

$$\lambda \begin{bmatrix} \hat{m} \\ \hat{c} \\ \hat{a} \end{bmatrix} = A(k) \begin{bmatrix} \hat{m} \\ \hat{c} \\ \hat{a} \end{bmatrix},$$

with

$$A(k) = \begin{bmatrix} -k^2 D - ra_0 & \frac{k^2\chi}{(1+\alpha a_0)^2} & 0 \\ \frac{1}{1+\beta a_0} & -1-k^2 & -\frac{\beta}{(1+\beta a_0)^2} \\ \frac{1}{(1+\beta a_0)\tau} & 0 & -\frac{k^2}{\tau} - \left(\frac{\beta}{(1+\beta a_0)^2\tau} + \frac{1}{\tau}\right) \end{bmatrix} = -k^2\mathcal{D} + \mathcal{K}. \tag{3.2}$$

According to the classical Turing analysis, if $\mathrm{Re}(\lambda) < 0$ for all eigenvalues λ of $A(k)$ and for all ks, then the homogeneous steady state P^* is stable. Otherwise, if for a given k there exists an eigenvalue $\lambda(k)$ of $A(k)$ such that $\mathrm{Re}(\lambda) > 0$, then spatially periodic perturbations of the homogeneous state with wavelength $2\pi/k$ may grow exponentially in time, making the equilibrium unstable. In particular, if the imaginary part of the unstable eigenvalue λ is zero, then Turing instability occurs; alternatively, if $\mathrm{Im}\{\lambda\} \neq 0$, a wave instability takes place.

In the absence of spatial effects, for $k = 0$, all the eigenvalues are negative: this implies that, in the absence of diffusion and chemotaxis, the homogeneous steady state P^* is linearly stable. We want to determine whether the inclusion of the linear diffusion or chemotaxis can destabilize the homogeneous equilibrium P^*, thus generating stationary or oscillatory instability. In the following theorem we prove that the linear diffusion terms, without the chemotaxis, are not able to destabilize P^*.

Theorem 3.1. *If $\chi = 0$, then P^*, the homogeneous equilibrium of system (2.4), is linearly stable.*

Proof. $\mathcal{K}$ is a stable matrix, i.e., by definition, the real part of all the eigenvalues of $\mathcal{K}$ is negative. Moreover, it can be easily seen that all the signed principal minors (see Definition 2. in [14]) of $\mathcal{K}$ are nonnegative; this implies, by Theorem 4. in [14], that $\mathcal{K}$ is a strongly stable matrix, i.e., by definition, that for all $\overline{D} = \mathrm{diag}(d_1, d_2, d_3)$ real, diagonal and positive semidefinite matrix, the matrix $\mathcal{K} - \overline{D}$ is stable. If $\chi = 0$ the matrix $\mathcal{D}$ defined by (3.1) is a real, diagonal and positive semidefinite matrix; then for all k, the matrix $\mathcal{K} - k^2\mathcal{D}$ is stable, which concludes the proof. ∎

From the previous result, it follows that for system (2.4) the chemotaxis is the only potentially destabilizing mechanism so that, hereafter, we shall assume $\chi \neq 0$. In what follows, we shall state the conditions leading to instability for $k \neq 0$.

3.1. Turing and wave instability. In this subsection we shall state some theorems giving the necessary and sufficient conditions for the occurrence of Turing and wave instability for system (2.4). We set $K := k^2$.

Let $\mathcal{P}(\lambda) = \lambda^3 + N(K)\lambda^2 + P(K)\lambda + Q(K)$ be the characteristic polynomial of (3.2), where $N(K), P(K)$ and $Q(K)$ are polynomials in K, whose explicit expressions are reported in section SM1, eqs. (SM1.1)-(SM1.3).

The Routh-Hurwitz criterion states that the all the roots of P have negative real part if and only if the following conditions hold:

$$1) N(K) > 0, \qquad 2) Q(K) > 0 \text{ and} \qquad 3) R(K) := N(K)P(K) - Q(K) > 0.$$

The first condition is always satisfied. In fact, $N(K) = -tr(A)$, and one immediately recognizes that the polynomial $N(K)$ is positive for all choices of the parameters and for all Ks.

Given that the first condition is satisfied, the second condition's violation corresponds to the emergence of a real positive root, which generates Turing instability. From the analysis of the polynomial Q it is possible to obtain a critical value χ_T such that for $\chi > \chi_T$, $Q(K) < 0$ in some range $[K_1, K_2]$, with $K_1 > 0$. This is the content of Theorem 3.2 below, whose proof is in section SM1.

Theorem 3.2 (Conditions for Turing instability). *There exist a critical value $\chi_T > 0$ such that, at $\chi = \chi_T$, system (2.4) undergoes a Turing bifurcation.*

The third condition's violation is not sufficient to ensure the emergence of wave instability. Indeed, the conditions $N > 0$, $Q > 0$ and $R < 0$ ensure the existence of a couple of roots with positive real parts, but we do not know whether they are complex. To have a wave instability, a

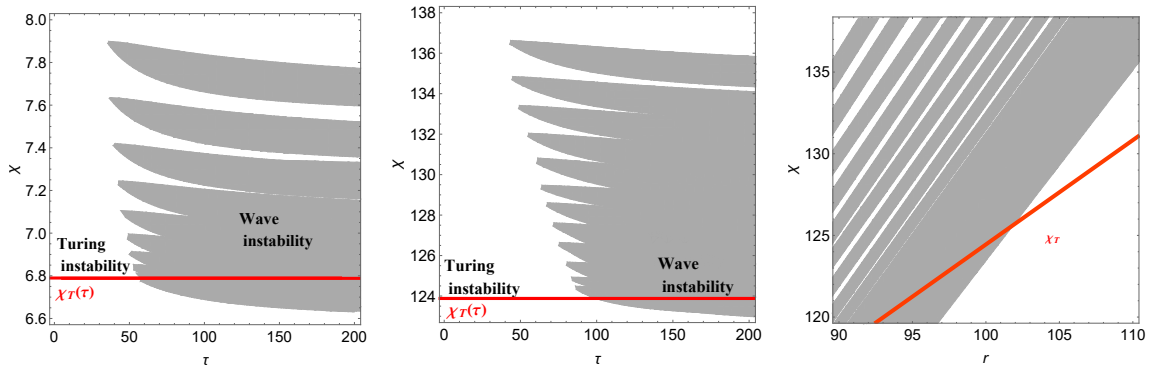

(a) (b) (c)

Figure 1: Instability regions for system (2.4): the red solid line $\chi_T(\tau)$ represents the bifurcation curve above which a Turing instability can be excited. The shaded areas represent the regions where a wave instability can occur. Parameters are fixed as follows: $D = 0.9, \alpha = 0.01, \beta = 0.1$. (a)-(b): (τ, χ)-plane for $r = 2.4$ and $r = 100$, respectively. (c): (r, χ)-plane for $\tau = 100$.

further condition involving the Bezoutiant matrix is necessary. This is the content of Theorem 3.3 below. The proofs, together with the definition of the Bezoutiant matrix is given in section SM1.

Theorem 3.3 (Conditions for wave instability). *The system (2.4) admits a wave instability if and only if there exists $K > 0$, compatible with the boundary conditions, such that:*

$$(i)\, Q(K) > 0, \qquad (ii)\, det(B(K)) < 0, \qquad (iii)\, R(K) < 0, \tag{3.3}$$

where $B(K)$ is the Bezoutiant matrix associated to the characteristic polynomial $\mathcal{P}(\lambda)$.

We shall study the occurrence of Turing and wave instabilities in system (2.4) mainly focusing on the variation of three parameters, namely the activation rate of macrophages r, the chemotactic coefficient χ and the time scale of the cytokine's dynamics τ, while keeping all the other parameters fixed. Concerning the other parameters, see Table 2, we shall fix the $D = 0.9$, $\rho = 1$, while the receptor-binding constant α and the inhibition rate β will be chosen to assume intermediate values among those reported in the medical literature. Using Theorems 3.2 and 3.3 one can determine the regions of the parameters space (r, τ, χ) in which either one of Turing or wave instability occurs.

In Figures 1a and 1b, we have fixed the value of r (equal to $r = 2.4$ and $r = 100$, respectively) and plotted in the (τ, χ)-plane Turing bifurcation curve $\chi_T(\tau)$, represented by the solid red line above which system (2.4) displays a Turing instability, and wave instability regions, represented by the grey regions; in Figure 1c the instability regions are plotted in the (r, χ)-plane for a fixed value of $\tau = 100$. Therefore, the points of the parameter space chosen within the grey regions lying above the Turing bifurcation curve $\chi_T(\tau)$ correspond to a parameters' choice for which both Turing and wave instability can occur, the linear analysis being unable to predict which instability will prevail in the outcoming solution.

From Figures 1a and 1b, we notice that the threshold value of the chemotactic coefficient for the occurrence of Turing patterns, $\chi_T(\tau)$, is indeed independent on τ: biologically, this implies that if the chemotaxis is sufficiently strong, stationary aggregates corresponding to persistent foci of inflammatory activity may form independently from the time-scale of the anti-inflammatory response. Conversely, wave instability, which corresponds to the insurgence of structures whose local density oscillates in time, is significantly affected by the value of τ: oscillations are favored by moderate and high values of τ, while they do not occur for τ small, see Figures 1a and 1b. Therefore, in the case of a wave instability, if the anti-inflammatory mechanism sets in with a delay sufficient to permit the development of a fully inflammatory response, then a temporary resolution of the inflammation is possible. This scenario is consistent with the reported periodic-in-time appearance of localized skin eruptions, known as Recurrent Erythema Multiforme (REM) [75, 93, 48], an acute, self-limited, inflammatory disease of unknown etiological attribution.

Moreover, from the comparison of Figures 1a and 1b, we can discern the effect of varying the parameter r on the instabilities. A higher value of the activation rate r implies that both Turing bifurcation threshold $\chi_T(\tau)$ and wave instability regions are shifted upwards. This agrees with the expectation that an increased activation rate favors the stability of the homogeneous state, consequently requiring a higher chemotactic strength for aggregation. The influence of r on the formation of stationary and oscillatory localized inflammation can be easily evinced also from Figure 1c: we see that, for a fixed value of χ, the homogeneous steady state P^* is stable when r is large and that it loses stability as r decreases.

The three Figures 1a to 1c also highlight which one of the two *competing* instabilities first sets in as χ is increased, showing that the prior occurrence of a Turing or of a wave instability depends on both τ and r. In fact, from Figures 1a and 1b one sees that very small values of τ favor stationary structures, while high values of τ favor the excitation of a wave instability; the threshold value of τ depends on the value of r.

In Figure 1c, where τ has been fixed, one can observe that increasing the value of r, Turing bifurcation is privileged with respect to wave instability.

To conclude this section, in Figures 2a to 2c, we present some numerical simulations corresponding to the different scenarios supported by the model; in all cases, the assigned initial condition is a random perturbation of the homogeneous equilibrium on the spatial interval $[0, 2\pi\sqrt{5}]$ (corresponding to a physical domain of about $1.5cm$-length). Figure 2a shows the spatio-temporal distribution of macrophages corresponding to Turing patterns; Figure 2b displays the macrophages density for a parameter set corresponding to a wave instability. In Figure 2b, we notice that the frequency of the temporal oscillations is compatible with the medical observations, reporting that REM is characterized by the recurrent appearance of distinctive target lesions with a 6.2 mean number of episodes per year. The close-up of Figure 2b, plotted in Figure 2c, in fact, shows the absence of localized inflammatory activity in the time interval elapsing between two consecutive attacks. Hence, the proposed model provides a mechanism that can explain the still unexplained origin of recurrent inflammations.

In all the simulations presented in this paper, we have adopted a second-order Runge-Kutta time-stepping scheme and, for space discretization, a Fourier spectral scheme. We have enforced the no-flux boundary conditions through the use of a cosine-Fourier transform. For the 1D simulations, 256 modes have given enough spatial resolution to obtain numerical

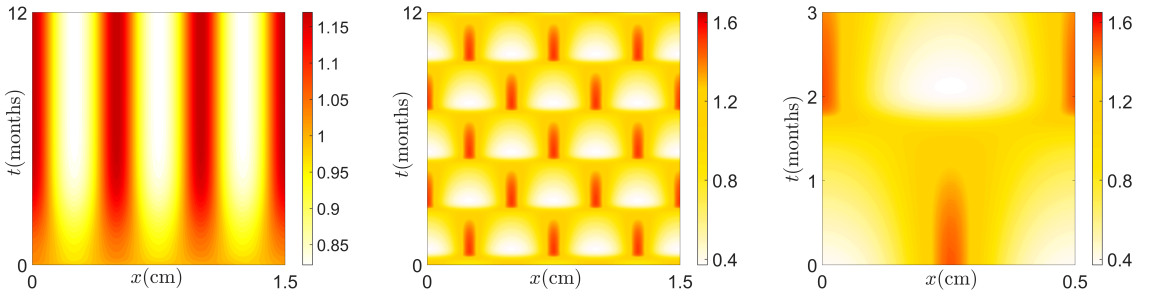

(a) (b) (c)

Figure 2: (a): Spatio-temporal evolution of m. The parameters are as in Figure 1 and $(r, \tau, \chi) = (2.4, 30, 6.9)$, corresponding to a Turing instability. (b): Spatio-temporal evolution of m. The parameters are as in Figure 1 and $(r, \tau, \chi) = (2.4, 200, 6.75)$, corresponding to a wave instability. (c): Close-up of (b)

convergence.

4. Weakly nonlinear analysis. In this section, we shall develop a weakly nonlinear analysis close to the uniform steady-state P^* based on the method of multiple scales [97, 26, 27, 29, 13, 65] to predict the amplitude and the shape of Turing pattern.

Upon defining $\mathbf{w} = (m-1, c-a_0, a-a_0)^T$ and separating the linear and the nonlinear part, we rewrite system (2.4) in the following form:

$$\begin{aligned}\partial_t \mathbf{w} =& \mathcal{L}^\chi \mathbf{w} + \nabla \cdot \mathcal{Q}_D^\chi(\mathbf{w}, \nabla\mathbf{w}) + \frac{1}{2}\mathcal{Q}_K(\mathbf{w}, \mathbf{w}) + \nabla \cdot \mathcal{C}_D^\chi(\mathbf{w}, \mathbf{w}, \nabla\mathbf{w}) \\ &+ \mathcal{C}_K(\mathbf{w}, \mathbf{w}, \mathbf{w}) + \nabla \cdot \mathcal{T}_D^\chi(\mathbf{w}, \mathbf{w}, \mathbf{w}, \nabla\mathbf{w}) + \mathcal{T}_K(\mathbf{w}, \mathbf{w}, \mathbf{w}, \mathbf{w}) \\ &+ \nabla \cdot \mathcal{P}_D^\chi(\mathbf{w}, \mathbf{w}, \mathbf{w}, \mathbf{w}, \nabla\mathbf{w}) + \mathcal{P}_K(\mathbf{w}, \mathbf{w}, \mathbf{w}, \mathbf{w}, \mathbf{w});\end{aligned} \tag{4.1}$$

where in the operators $\mathcal{L}^\chi$, $\mathcal{Q}_D^\chi$, $\mathcal{C}_D^\chi$, $\mathcal{T}_D^\chi$ and $\mathcal{P}_D^\chi$ we have stressed the dependency on the bifurcation parameter χ. The linear operator $\mathcal{L}^\chi$ is defined as $\mathcal{L}^\chi = \mathcal{D}^\chi\Delta + \mathcal{K}$ where $\mathcal{D}^\chi$ and $\mathcal{K}$ are defined in (3.1). The action of the multilinear operators is given in subsection SM2.1.

We define the small control parameter $\varepsilon^2 = (\chi - \chi_c)/\chi_c$ and expand the solution of system (4.1) and the bifurcation parameter χ in ε:

$$\mathbf{w} = \varepsilon\mathbf{w}_1 + \varepsilon^2\mathbf{w}_2 + \varepsilon^3\mathbf{w}_3, \tag{4.2}$$

$$\chi = \chi_c + \varepsilon^2\chi^{(2)} + O(\varepsilon^4). \tag{4.3}$$

Performing a weakly nonlinear analysis up to $O(\varepsilon^3)$, we obtain the following Stuart-Landau equation for the amplitude $A(T)$:

$$\frac{dA}{dT} = \sigma A - LA^3. \tag{4.4}$$

The details of the derivation of (4.4) are given in subsection SM2.2, while σ and L are given in (SM2.10). The coefficient σ, in the region of Turing instability, is always positive. On the other hand, L can have either sign. Therefore the dynamics of the Stuart-Landau equation (4.4) can be classified into two qualitatively different cases: the supercritical case, when L is positive, and the subcritical case, for L negative.

In the supercritical case, there exists a stable equilibrium solution of the Stuart-Landau equation (4.4), namely $A_\infty = \sqrt{\sigma/L}$, that represents the asymptotic value of the amplitude of the pattern. According to the weakly nonlinear theory, the asymptotic behavior of the solution is given by:

$$\mathbf{w} = \varepsilon \boldsymbol{\eta} \sqrt{\frac{\sigma}{L}} \cos(k_c x) + \varepsilon^2 \frac{\sigma}{L} (\mathbf{w}_{20} + \mathbf{w}_{22} \cos(2k_c x)) + O(\varepsilon^3), \tag{4.5}$$

where k_c is the critical wavenumber.

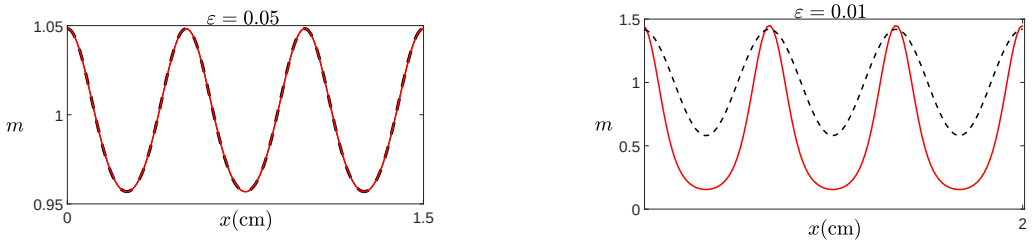

(a) (b)

Figure 3: Comparison between the weakly nonlinear solution (dotted line) and the numerical solution of system (2.4) (solid line). (a): Supercritical case: the parameters are $D = 0.9$, $r = 5$, $\alpha = 0.01$, $\beta = 0.1$, $\tau = 30$ on the spatial interval $[0, 2\pi\sqrt{1.3}]$ (corresponding to a physical domain of about $1.14cm$-length). With this choice of the parameters, one has $\chi_c = 6.779$, $k_c = 2.99$, $\varepsilon = 0.05$. (b): Subcritical case: the parameters are $D = 0.9$, $r = 0.1$, $\alpha = 1$, $\beta = 0.4$, $\tau = 30$ on the spatial interval $[0, 6\pi]$ (corresponding to a physical domain of about $2cm$-length). With this choice of the parameters one has $\chi_c = 1.606$, $k_c = 0.95$, $\varepsilon = 0.01$

In Figure 3a we show a comparison between the stationary solution (4.5) predicted by the weakly nonlinear analysis and the Turing pattern, computed using a numerical spectral scheme and reached starting from a random perturbation of the uniform steady state. The two solutions display an excellent agreement, the L^2-norm of the distance between the numerical solution and the weakly nonlinear solution being consistent with the $O(\varepsilon^3)$ approximation.

In the subcritical case the Landau coefficient L is negative, so that the equation (4.4) is not able to predict the amplitude of the pattern. We therefore have to push the weakly nonlinear expansion to the fifth order to obtain the following quintic Stuart-Landau equation for the amplitude $A(T)$:

$$\frac{dA}{dT} = \bar{\sigma} A - \bar{L} A^3 + \bar{Q} A^5, \tag{4.6}$$

The details of the analysis are given in subsection SM2.3. In the subcritical case, namely when $\bar{\sigma} > 0, \bar{L} < 0$, and $\bar{Q} < 0$, Equation (4.6) admits two real stable equilibria, $A_{\infty,\pm} = \sqrt{\frac{\bar{L} - \sqrt{\bar{L}^2 - 4\bar{\sigma}\bar{Q}}}{2\bar{Q}}}$, which represent the asymptotic values of the amplitude A of Turing pattern. In this case, the amplitude A is $O(\varepsilon^{-1})$ and, consequently, the emerging pattern is an $O(1)$ perturbation of the equilibrium. Therefore, the solution obtained through the weakly nonlinear analysis may fail to capture the quantitative features of the emerging structures. For this reason, in general we cannot expect a good agreement between the asymptotic and the numerical solutions, as it happens in the supercritical case. Nevertheless, the simulation reported in Figure 3b shows that, close to the critical threshold, the asymptotic solution still closely reproduces the expected pattern.

5. Complex behavior: coarsening dynamics, oscillations and chaos. In this section, we shall carry a detailed numerical investigation of system (2.4), aimed at showing that the presence of the cell kinetic term is able to induce complex dynamics. Therefore, in the present section, the main interest is probing the activation term's effect on the solutions rather than reproducing observed phenomena.

The emergence of oscillatory patterns and spatio-temporal chaotic solutions for chemotaxis systems of Keller-Segel-type with cell-growth terms had already been observed in [63, 64, 91]. We shall see that the presence in system (2.4) of the cell-growth term is crucial for the appearance, as the parameter χ is varied, of a sequence of successive bifurcations leading to time-periodic patterns and spatio-temporal chaos.

To follow the sequence of bifurcations, we fix all the parameters except χ, and track the emergence of different solutions, as χ is varied, adopting the same procedure used in [64], namely:

1. We initialize the procedure selecting a value of $\chi < \chi_T$, (where χ_T is the critical value for Turing instability), and assign a random perturbation of the homogeneous steady state P^* as initial condition;
2. system (2.4) is solved numerically until the time $T = T_{\text{end}}$, at which the system has reached a stable configuration, i.e., up to the time when the final state can be classified (either as an equilibrium, or as a periodic solution, or a chaotic state);
3. we slightly increase the value of χ and perform a new simulation, starting from an initial condition that is a small random perturbation of the solution attained at the previous step. We then return to step 2.

To track distinct branches originating at bifurcation points, we repeat step 3 for the same value of χ, starting from different random perturbations of the solution obtained for the previous value of χ at $t = T_{\text{end}}$.

5.1. Coarsening dynamics: the $r = 0$ case. We shall begin the bifurcation analysis by first considering the case $r = 0$. Namely, in this Subsection, we shall exclude from the reaction kinetics the macrophage activation term: we shall see that the system supports metastable stationary patterns, and we shall provide the mathematical justification for the observed *coarsening dynamics*. We recall that, in the case $r = 0$, the equilibrium value of the macrophages is fixed by the initial conditions so that the corresponding homogeneous steady state is always marginally stable.

In Figure 4, we report the results of our first simulation. For the chosen parameter set, the linear stability analysis predicts that for $\chi > \chi_T = 1.617$, any arbitrarily small positive wavenumber's growth rate is greater than zero. At $\chi_{T,1/2} = 1.868$, the first wavenumber admitted by the boundary conditions, namely $k = 1/2$, is destabilized. The simulation, in fact, reveals that for values of the bifurcation parameter higher than $\chi_{T,1/2}$, the cells population aggregates in a unique stable peak, whose amplitude grows, concentrating on one end of the domain, as the chemotactic response increases.

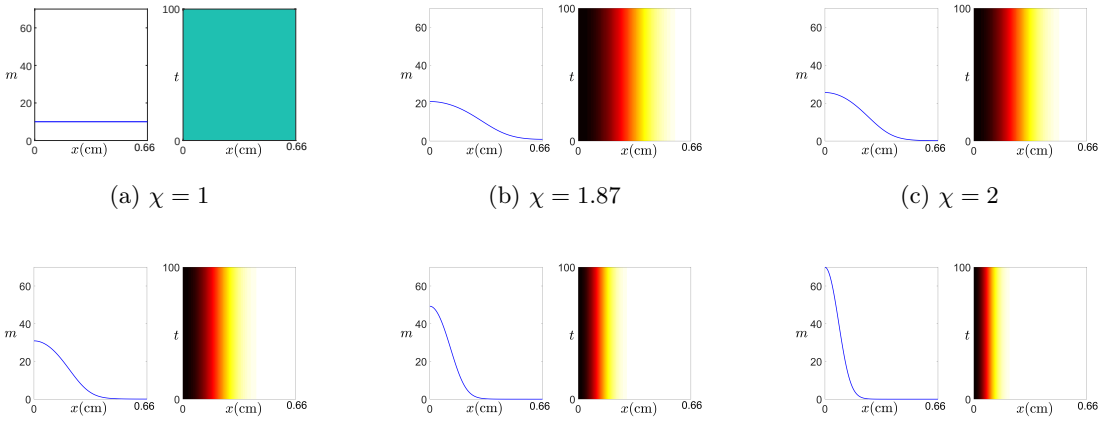

(a) $\chi = 1$ (b) $\chi = 1.87$ (c) $\chi = 2$

(d) $\chi = 2.2$ (e) $\chi = 3$ (f) $\chi = 4$

Figure 4: Numerical bifurcation analysis of system (2.4), revealing a stable branch of equilibria. The spatial interval is $[0, 2\pi]$ (corresponding to a physical domain of about $0.66cm$-length), while the parameters values are $r = 0, D = 0.45, \alpha = 0.5, \beta = 0.4, \tau = 10, m_0 = 10$. The critical value for χ is $\chi_T = 1.617$, while $\chi_{T,1/2} = 1.868$, where $\chi_{T,1/2}$ is the bifurcation value of the mode $k = 1/2$, the first admitted by the boundary conditions. In each subfigure we plot the profile (left) and the space-time (right) density of the macrophage species. In absence of a cell activation term we observe aggregating dynamics leading to the formation of a stable stationary structure.

In Figure 5, we report a numerical simulation where we have chosen a larger spatial domain which can admit, therefore, as stable solutions patterns with many peaks. In this case, one can observe the phenomenon of merging dynamics [74, 63, 64], also referred to as *coarsening dynamics*: the system, starting from a perturbation of the homogeneous equilibrium, evolves towards a multi-peak solution that appears stationary in time; nevertheless, on a longer time scale, one observes further aggregation of the structures, due to the strong chemotactic attraction between adjacent peaks. Therefore, merging of the structures corresponds to transient dynamics along metastable multipeaked solutions. A detailed mathematical investigation of the asymptotic dynamics expected in Figure 5 is beyond this paper's scope. However, in the next subsection, we shall mathematically justify the observed transitions between metastable states. We notice that the absence of the activation term prevents the formation of new ag-

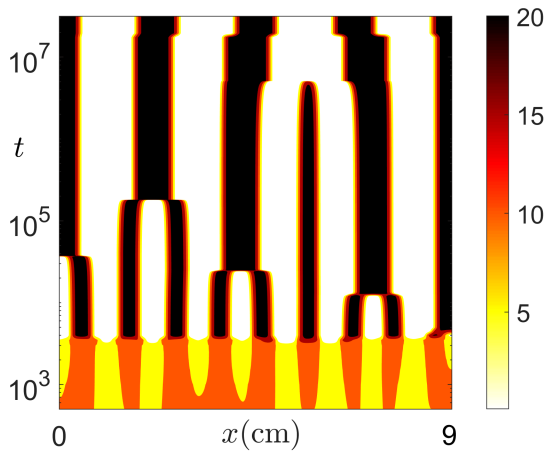

Figure 5: Spatio-temporal evolution of the species m of system (2.4) with zero growth ($r = 0$), showing merging dynamics. The numerical values of the parameters are $r = 0, \chi = 1.75, D = 0.45, \alpha = 0.5, \beta = 0.4, \tau = 30, m_0 = 10$, so that $\chi_T = 1.617$ and $\chi_{T,\frac{1}{2}} = 1.6326$, where $\chi_{T,\frac{1}{2}}$ is the bifurcation value of the first mode admitted by the boundary conditions.

glomerates, precluding the insurgence of the emerging phase that is observed when $r \neq 0$, see subsection 5.2.

Finally, we have tested other parameter sets and, as long as $r = 0$, spatio-temporal irregularity of the solutions has not been detected: therefore, our simulations strongly suggest that, in the absence of a cell activation term, complex dynamics are excluded.

5.1.1. Eckhaus instability. The wavenumber adjustments observed in Figure 5 are due to a secondary instability, known as Eckhaus instability. We shall see that our system shows the typical bifurcations sequence one encounters in the Eckhaus scenario, reported in Figure 6, and that can be described as follows. Increasing χ beyond $\chi_{T,1/2}$, in addition to the first destabilized mode, other pure-mode patterns, characterized by different wavenumbers, progressively bifurcate from the homogeneous equilibrium through primary bifurcations. Each branch of patterned solutions, except the first one, is unstable at the primary bifurcation and undergoes a sequence of secondary bifurcations; the last one, occurring at the Eckhaus threshold, stabilizes the branch. Moreover, at each secondary bifurcation, a pair of unstable mixed-modes states bifurcates subcritically. Therefore, for values of χ sufficiently bigger than $\chi_{T,1/2}$, several pure- and mixed-mode solutions with different stability properties may coexist. Perturbations along the pattern's longitudinal direction can then induce a wavelength-changing process, inserting or removing stripes in the emerging solution. The above-described scenario has been studied in great detail in [86].

To justify the above described scenario, in what follows we shall study the eM135810RRf4bM135810RRf4bxistenc

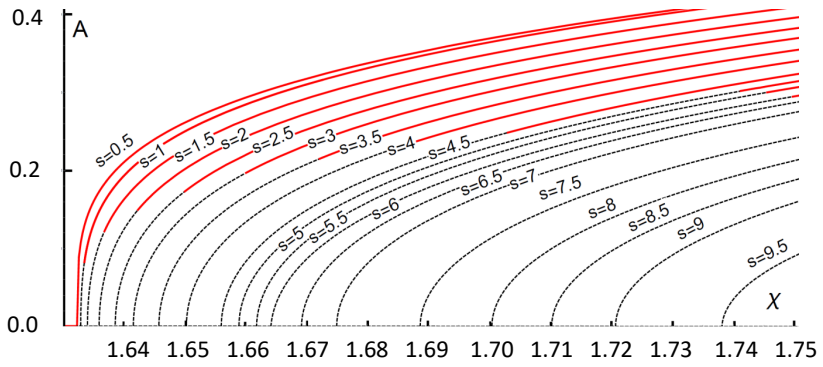

Figure 6: Bifurcation diagram of stationary solutions of (2.4) illustrating the Eckhaus instability. The amplitude A of the stationary solutions to (2.4) is plotted versus the bifurcation parameter χ. Solid (dashed) lines correspond to stable (unstable) branches of solutions. Pure-mode branches with different wavenumbers bifurcate supercritically from the homogeneous steady state: all branches except the first are unstable at onset. Each pure-mode branch undergoes a sequence of bifurcations, the last of which, occurring at the Eckhaus threshold, stabilizes the branch.

and stability properties of the striped patterns and determine the corresponding bifurcation thresholds. This analysis will allow us to discern, for a fixed value of the control parameter, which modes are stable and, consequently, to rule out from the asymptotic solutions of (2.4) the unstable modes that may grow in the initial and intermediate stages of the dynamics.

We fix the small control parameter $\varepsilon^2 = (\chi - \chi_c)/\chi_c$ and, using the same method adopted in section 4, perform a multiple-scale analysis. By defining the slowly varying variables: $X = \varepsilon x, T = \varepsilon^2 t$, we obtain the following Ginzburg-Landau equation for the amplitude $\mathcal{A} = \mathcal{A}(X, T)$ of the pattern:

$$\frac{\partial \mathcal{A}}{\partial T} = \sigma \mathcal{A} - \gamma |\mathcal{A}|^2 \mathcal{A} + \nu^2 \frac{\partial^2 \mathcal{A}}{\partial X^2}, \tag{5.1}$$

where the coeffients σ, γ, ν are written in terms of the parameters of the original system (2.4). The solution to (4.1) then reads:

$$\mathbf{w} = 2\varepsilon \,\mathrm{Re}[\mathcal{A}(X, T) e^{ik_T x}] + O(\varepsilon^2). \tag{5.2}$$

Upon rescaling all the variables, (5.1) can be rewritten in the following form:

$$\frac{\partial A}{\partial \tilde{t}} = \mu A - |A|^2 A + \frac{\partial^2 A}{\partial \tilde{x}^2}, \tag{5.3}$$

where $\tilde{x} \in [0, \pi]$. Hence, the rescaled solution of (4.1) writes as:

548 (5.4) $$\tilde{\mathbf{w}} = 2\varepsilon\,\mathrm{Re}[A(\tilde{x},\tilde{t})e^{iQ_T\tilde{x}}] + O(\varepsilon^2),$$

549 where Q_T is the rescaled critical Turing mode, and the base Turing pattern is recovered when
550 $A(\tilde{x},\tilde{t}) = \sqrt{\mu}$ (for more details, see [8]). We now look for nontrivial (beside $A = 0$ or $A = \sqrt{\mu}$)
551 solutions to (5.3), of the form Ce^{iQx}, where C is a constant, and we have omitted the tilde for
552 notational simplicity. One finds that, for $\mu > Q^2$, there exist the following steady solutions to
553 (5.3):

554 (5.5) $$A = \sqrt{\mu - Q^2}e^{iQx},$$

555 that bifurcate supercritically from $A = 0$ at $\mu = Q^2$. The fact that (5.4) must satisfy the
556 boundary conditions imposes that are admissible only those values of Q such that $Q_T + Q$ is
557 an integer or semi-integer. To determine the linear stability of the solutions (5.5), we add a
558 perturbation of the form

559 (5.6) $$a(x,t) = e^{\Lambda t}e^{iQx}(\alpha e^{ikx} + \beta e^{-ikx}),$$

560 with α and β real and $k \neq 0$. A standard linearization procedure, whose details can be found
561 in [86], gives the eigenvalues

562 (5.7) $$\Lambda_{\pm}(Q,k,\mu) = -(\mu - Q^2 + k^2) \pm \sqrt{(\mu - Q^2)^2 + (2kQ)^2},$$

563 and the stability conditions

564 (5.8) $$\mu > \mu_E(Q) = 3Q^2 - \frac{1}{2},$$

565 yielding, for each branch with wavenumber $Q_T + Q$, the Eckhaus bifurcation value.
566 Based on the above analysis, we now consider the dynamical transitions showed in Figure 5.
567 We assign an integer or a semi-integer s to the pattern with s spatial oscillations (stripes), and
568 denote its amplitude with $A_s = \sqrt{\mu - Q_s^2}\,e^{iQ_s x}$. For each s-pattern, we compute the primary
569 bifurcation point $\mu_s = Q_s^2$ and the Eckhaus bifurcation threshold $\mu_{Es} = 3Q_s^2 - \frac{1}{2}$. As μ is
570 a function of the control parameter χ, we derive the corresponding thresholds χ_s and χ_{Es},
571 expressing the primary bifurcation and the Eckhaus bifurcation values of χ, respectively; for
572 each s-pattern with $s = 0.5, 1, \ldots, 9$, the numerical values are listed in Table 3. In Table 3,
573 we have also reported the corresponding eigenvalue Λ_{+s}, computed at $\chi = 1.75$, which is the
574 value of the chemotactic coefficient chosen in the simulation reported in Figure 5.
575 From Table 3, one sees that the value $\chi = 1.75$ selected in the simulations of Figure 5 is
576 greater than the primary bifurcation threshold for all the s-pure mode solutions reported in
577 the Table. Therefore, at $\chi = 1.75$, all the pure mode branches with $0.5 \leq s \leq 9$ have already
578 bifurcated from the homogeneous state and are *active modes*, namely, they are stationary
579 solutions of (2.4). However, the pure mode solutions with $6.5 \leq s \leq 9$ have an Eckhaus stability
580 threshold χ_{Es} higher than 1.75 and are consequently unstable, a fact also confirmed by the
581 positive value of their corresponding eigenvalue Λ_{+s}. Conversely, the pure solution branches
582 with $0.5 \leq s \leq 6$ have Eckhaus stability threshold χ_{Es} below 1.75 and negative eigenvalue Λ_{+s}

s	χ_s	χ_{Es}	$\Lambda_{+s} * 10^{-7}$	s	χ_s	χ_{Es}	$\Lambda_{+s} * 10^{-7}$
0.5	1.6326	–	−3.4758	5	1.6603	1.7428	−1.1151
1	1.6329	1.6335	−3.4539	5.5	1.6605	1.7459	−0.91076
1.5	1.6340	1.6368	−3.3875	6	1.6609	1.7490	−0.7555
2	1.6359	1.6423	−3.2741	6.5	1.6693	1.7742	2.2119
2.5	1.6384	1.6500	−3.1089	7	1.6747	1.8189	4.2891
3	1.6418	1.6599	−2.8852	7.5	1.6883	1.8311	7.4459
3.5	1.6458	1.6721	−2.5924	8	1.7047	1.8807	12.730
4	1.6506	1.6864	−2.2159	8.5	1.7101	1.8968	23.085
4.5	1.6561	1.7030	−1.7340	9	1.7222	1.9329	49.641

Table 3: Existence and Eckhaus stability thresholds of s-patterns of system (2.4) with parameter values given in Figure 5. χ_s is the primary bifurcation point above which the pattern with s stripes bifurcates from the homogeneous steady state. The secondary bifurcation value χ_{sE} yields the threshold beyond which the s-stripes solution becomes Eckhaus-stable. For each s-pure mode, the eigenvalue Λ_{+s} is computed at the value $\chi = 1.75$ used in the simulations of Figure 5.

and, accordingly, are linearly stable patterns. Therefore, given that the initial condition is a small random perturbation of the homogeneous equilibrium, after that the rapidly decaying inactive modes with $s > 9$ have subsided, system (2.4) evolves through a sequence of long-lived transient states whose spectrum is a superposition of the active modes. In the first metastable configuration, the spectrum's predominant component is the active mode with the smallest amplitude (corresponding to $s = 9$) that also has the smallest half-life. In the successive metastable configurations, pure-mode solutions of increasing amplitude and half-life prevail in the spectrum, resulting in the observed process of progressively longer transients, characterized by an increasingly smaller number of stripes in the solution profile. The dynamics ultimately converges towards the absorbing manifold generated by the Eckhaus-stable modes, as can be seen in the final state of Figure 5, whose spectrum is a superposition of the pure-mode solutions with $s \leq 6$. A forecast of the asymptotic solution would require a nonlinear analysis that takes into account the competition between the different Eckhaus-stable modes (see, for example, [25]), which will not be performed here.

5.2. Oscillations and chaos: the $r > 0$ case. We now consider the case $r > 0$: we show that the inclusion of a logistic-type kinetics term produces a wide variety of oscillatory and chaotic dynamics. In reaction-diffusion systems, these behaviors typically arise because of wave instability or interaction between Turing and Hopf instabilities; on the other hand, in the cases that we shall see below, oscillations occur in a parameter space's region where the linear stability analysis predicts neither Hopf nor wave instabilities, but only a pure Turing instability. We show two numerical experiments in which we investigate the behavior of the solution in both a supercritical, see Figure 7, and a subcritical Turing regime, see Figure 9.

In the first simulation, we have chosen the set of parameters indicated in Figure 7, for

which the linear stability analysis predicts that the homogeneous solution P^* becomes Turing unstable for $\chi > \chi_T = 16.55$, with most unstable wavenumber $k_T = 4$. Figure 7 describes the sequence of bifurcations by which the homogeneous solution (shown in Figure 7a) loses stability as $\chi > \chi_T$: the stationary pattern predicted by the linear analysis that develops for $\chi \gtrsim \chi_T$ (Figure 7b) persists, with the peaks becoming sharper, as χ is further increased (Figure 7c). Between $\chi = 17.6$ and $\chi = 17.65$, the Turing pattern becomes unstable, bifurcating to a time-periodic spatial pattern: the numerical simulation shown in Figure 7d reveals, at $\chi = 17.7$, the presence of an oscillating solution. Increasing the value of χ, the oscillation amplitude becomes larger further, see Figure 7e. Between $\chi = 18.2$ and $\chi = 18.25$, the periodic solution undergoes a period-doubling bifurcation, described by the doubling in the loop structure of the trajectories calculated at $x = \pi$, see Figure 7f; this is also confirmed by a Fourier analysis of the temporal behavior of the solutions that we do not report here. This new class of solutions remains stable up to $\chi = 18$; at $\chi = 18.1$, a small increment of the chemotactic term results in the periodic pattern to lose its stability with the appearance of an irregular spatio-temporal solution (Figure 7g). The chaotic solution is still present for an increased value of χ although, at $\chi = 18.5$, a time-periodic pattern with a different wavenumber ($k = 3.5$) appears, as shown in Figure 7h. This type of solution remains stable until $\chi = 18.6$, successively undergoing a torus bifurcation at $\chi = 18.625$, see Figure 7i. A further increase of χ induces the occurrence of spatio-temporal chaotic dynamics, see Figure 7j and Figure 7k; at $\chi = 18.8$, a stationary patter reappears, see Figure 7l.

As shown in Figure 8a, the dispersion relation (at $\chi = 17.7$, very close to the onset of oscillations) reveals that the critical mode $k_T = 4$ is linearly unstable, as it has a real positive eigenvalue, while its 1/2-subharmonic is stable, having complex eigenvalues with negative real part. Therefore, according to the linearized dynamics, only stationary structures should establish. However, as suggested by the analysis of the spectrum of the numerically computed solution (see Figure 8b), the oscillations in Figure 7d are to be ascribed to a resonance between the Turing mode, $k_T = 4$, and its 1/2 subharmonic: with increasing χ, in fact, there exists a critical value of the control parameter beyond which the instability triggers a nonlinear transfer of energy from the critical mode to the 1/2- mode, which begins to oscillate. As a result, at each spatial location the system oscillates with one frequency, but the presence of two unstable modes, k_T and $k_T/2$, shifts the maxima of the pattern one wavelength every half period of oscillation (see Figure 8c). In Figure 8d we report the anti-phase oscillations at two neighboring extrema.

In Figure 9 we present another numerical experiment: for the chosen parameter set, the linear stability analysis predicts that the homogeneous solution P^* becomes unstable for $\chi > \chi_T = 0.514$ with $k_T = 4.5$ most unstable wavenumber. Figure 9 describes a sequence in which the homogeneous solution (in Figure 9a) loses stability as $\chi > \chi_T$ to a stationary pattern (Figure 9b). This branch remains stable until $\chi = 0.565$, after which one observes the appearance of an irregular solution, characterized by a sequence of merging and emerging structures whose wavenumber oscillates between 4 and 5 (see Figure 9c). Increasing the chemotactic sensitivity, the system settles in a stationary-in-time pattern with a smaller wavenumber, as shown in Figure 9d. This transition is again found if we further increase χ: in Figure 9e an irregular solution is reported which is stabilized as $\chi = 0.67$ (Figure 9f) where a stationary pattern with a different wavenumber appears.

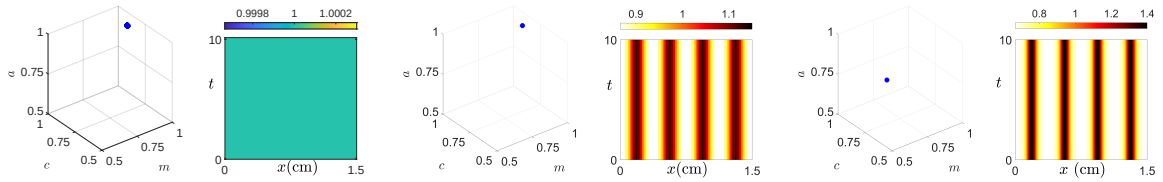

(a) $\chi = 16$ (b) $\chi = 16.7$ (c) $\chi = 17$

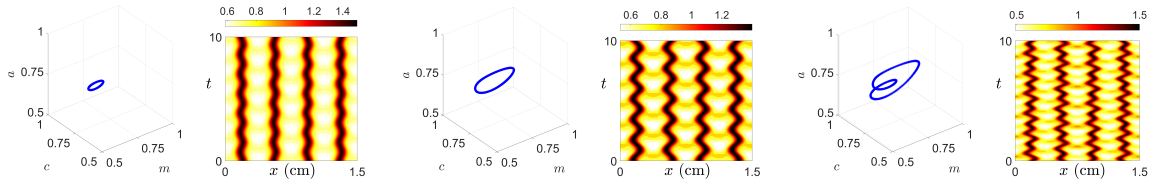

(d) $\chi = 17.7$ (e) $\chi = 18$ (f) $\chi = 18.03$

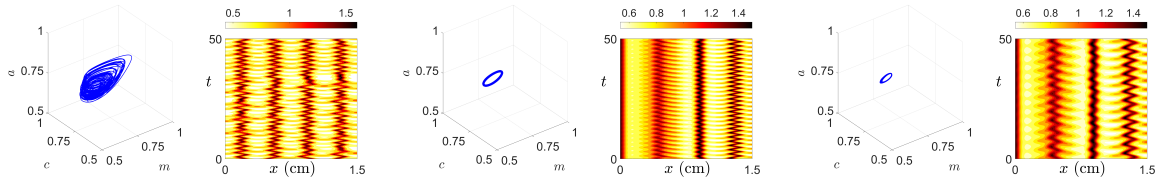

(g) $\chi = 18.1$ (h) $\chi = 18.5$ (i) $\chi = 18.625$

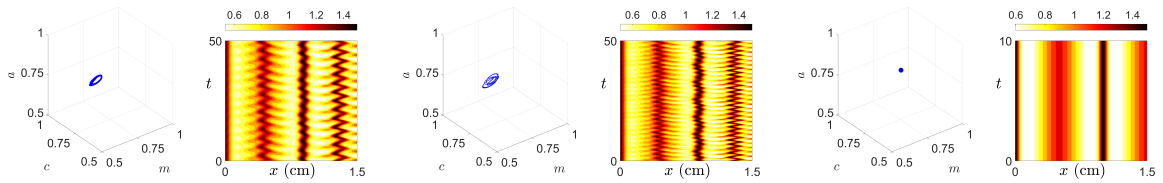

(j) $\chi = 18.63$ (k) $\chi = 18.635$ (l) $\chi = 18.8$

Figure 7: Numerical bifurcation analysis of system (2.4) showing transition to irregular spatio-temporal solutions on the spatial interval $[0, 2\pi\sqrt{5}]$ (corresponding to a physical domain of about $1.5cm$-length). The parameters are $r = 9, D = 0.9, \alpha = 0.01.\beta = 0.1, \tau = 30$. In each frame Figure 7a-Figure 7l, we plot the phase-space trajectories at the spatial location $x = L/2$ ($L = 1.5$ cm) (left), and the space-time snapshot of the macrophage density for $t > T_{\text{end}}$ (right)

In both the numerical experiments showed in Figures 7 and 9, as the chemotactic parameter is increased, we can observe: first, a transition of striped patterns towards chaotic solutions; second, the stabilization to stationary patterns with different wavenumbers. The increase of χ causes two different phenomena: first, the stationary solution undergoes destabilizing bifurcations, such as the subharmonic resonance reported in Figures 7d to 7k. Second, away from the bifurcation threshold, additional stationary solutions with different wavenumbers arise from the homogeneous state through a primary instability at χ_n and then stabilize through

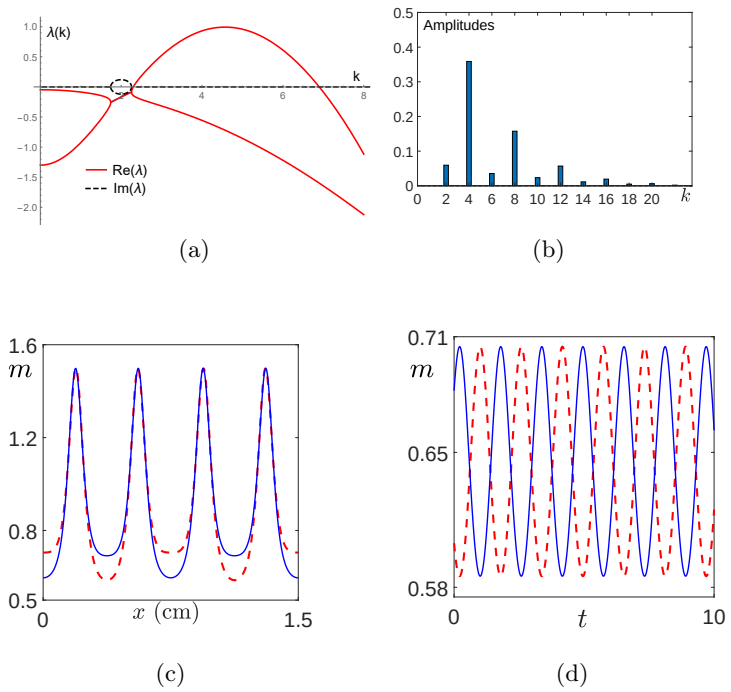

Figure 8: Out-of-phase oscillatory Turing pattern. The parameter values are chosen as in Figure 7d. Figure 8a: dispersion relation at the onset of oscillations showing the real and imaginary part of the eigenvalues, represented by solid and dashed lines respectively. The third eigenvalue is not represented here since it is always negative. Figure 8b: Fourier spectrum of the solution at the onset of oscillations showing excitation of the mode $k_c/2 = 2$. Figure 8c: the solid and dashed curves are two anti-phase patterns separated in time by $T/2 \simeq 0.8$. Figure 8d: the solid and dashed curves are two-phase oscillations at locations separated in space by $L/2$, where $L = 1.5$ is the length of the spatial domain.

an Eckhaus bifurcation at χ_{En}.

For the parameter set of Figure 7, with a procedure analogous to the one adopted in subsection 5.1.1, we have computed the bifurcation thresholds of the striped patterns involved in the numerical simulations in Figure 7. The results are listed in Table 4 and show that chaotic solutions stabilize when a stationary pattern becomes Eckhaus stable.

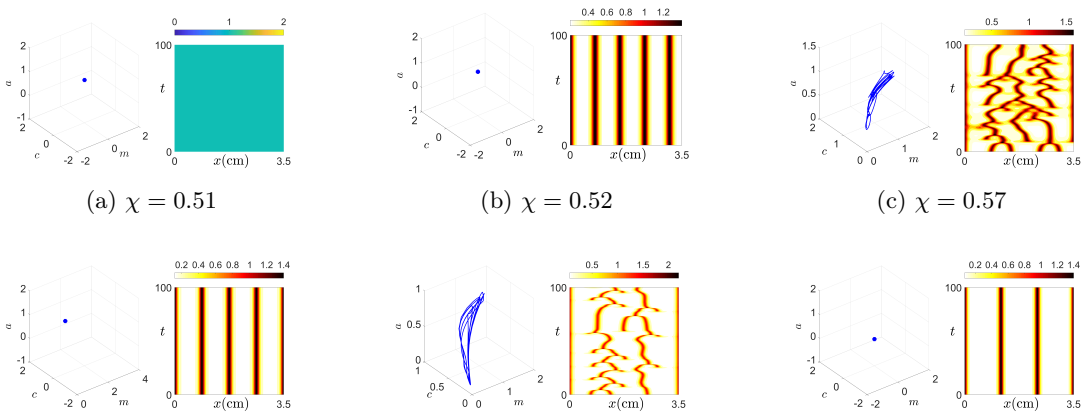

(a) $\chi = 0.51$ (b) $\chi = 0.52$ (c) $\chi = 0.57$

(d) $\chi = 0.58$ (e) $\chi = 0.66$ (f) $\chi = 0.67$

Figure 9: Numerical bifurcation analysis of system (2.4) on the spatial interval $[0, 2\pi\sqrt{30}]$ (corresponding to a physical domain of about $3.5cm$-length). The parameters are $r = 0.1, D = 0.9, \alpha = 0.1, \beta = 0.1, \tau = 30$. For each subfigure Figure 9a-Figure 9f, we plot the phase-space trajectories at the spatial location $x = \pi$ (left), and the space-time snapshot of the macrophage density (right)

n	χ_n	χ_{En}
3	17.4124	18.7466
3.5	16.8342	17.3119

Table 4: Existence and Eckhaus stability thresholds of striped pattern of system (2.4) with parameter values given in Figure 7. χ_n is the primary bifurcation point above which the pattern with n stripes bifurcates from the homogenous state. The secondary bifurcation value χ_{nE} represents the threshold beyond which the n-stripes solution becomes Eckhaus stable.

To conclude this section, we observe that the simulations of Figures 7 and 9 illustrate how the model (2.4) exhibits *critical* dynamics of the macrophages. In the jargon of statistical physics, a system is said to be at *criticality* when it operates in the proximity of a phase transition: a *critical point* in the phase space corresponds to a state at the edge between two different phases, each of whom is attained as a control parameter is varied below or above the transition value. When phase transitions separate a well-ordered state from a disordered one, the corresponding critical points are said to be *at the edge of chaos*. Since the $'90s$, the hypothesis of operating at criticality has been formulated for many living systems [54, 56], which would benefit from residing in this highly variable and adaptive dynamical regime and, therefore, would be evolutionarily selected for being tuned at the corresponding value of the control parameter. Auto-tuning at criticality of biological systems is known as *self-oganized criticality*, a concept that has been introduced in [4]. Hallmarks of criticality have

been recognized in enzyme kinetics [55], growth of bacterial populations [58], foraging in ant colonies [6], neuronal networks [7], auditory system [37]; whereas deviation from criticality could be the symptom or the cause of malfunctioning and pathology [35, 76, 79, 80].

Some recent works support the hypothesis of macrophage criticality, according to which operating in the proximity of a critical regime would be beneficial to optimize the functioning of the cells, namely, it would guarantee diversity of immune response yet maintaining homeostatic stability. On a subcellular length scale, [10, 88] detect the presence of phase transitions in biological membranes that directly imply a wide phenomenology of spontaneous lipid organization. Particularly, in [10] the authors give experimental evidence to the fact that the macrophage plasma membrane operates close to a critical point: in response to pro- and anti-inflammatory cytokine stimulation, the lipidic morphology of the membrane undergoes phase transitions that affect the membrane's receptors regulating macrophage activation. Besides, the authors show that changes in the macrophages concentration are also able to affect the membrane physical properties. Since the membrane operates close to criticality, by tuning the macrophage density, the immune system would realize a mechanism for efficient cell activity regulation. In [60] the investigation of critical behavior is performed on a mesoscopic scale that neglects the details of intracellular processes. The authors analyze several biological datasets of stimulated macrophage populations and estimate the corresponding information-based order parameters indicating differential gene expression. Their experiments show that, in response to pathogen-associated molecular patterns, macrophages exhibit dynamics in the critical regime at the boundary between order and chaos.

The simulations reported in Figures 7 and 9, show that the model (2.4) predicts the existence of regions in the parameter space where ordered states are immersed within spatio-temporal irregular solutions: a small variation of the control parameter induces a sequence of bifurcations through which the system alternately transits from well-ordered to less ordered configurations. For realistic values of the parameters, our model, therefore, reproduces critical behavior of the immune cells in extended areas of the parameter space. Large regions of criticality in the macrophage dynamics can also be figured out from inspection of Figure 1: in Figures 1a and 1b, there exist wide ranges of values of τ for which a small variation of the chemotactic coefficient χ determines the occurrence of sequentially alternating Turing/wave bifurcations, corresponding to alternate transitions from stationary to traveling agglomerates. A similar scenario is also depicted in Figure 1c, when one considers variations either in χ or in the macrophage activation rate r. From the modeling viewpoint, the presence of the cell activation term turns out to be essential to reproduce the presence of regions where complex dynamics is immersed in stable steady states, while absence of the reaction kinetics in the macrophage dynamics, as in the model presented in [66], results in a system characterized by too much stability, i.e. incapable of transitions to a disordered state.

6. 2D stationary radially symmetric solutions. In the present and the following section, we shall investigate the self-organization properties of system (2.4) on 2D domains. In this section, we shall perform a theoretical bifurcation analysis through which we shall classify different axisymmetric stationary patterns supported by the model. In the following section, we shall numerically simulate the full $2D$ system and show that the proposed model can successfully reproduce the formation of various inflammation patterns, as observed in several

cutaneous rashes.

To investigate the existence and stability of stationary radially symmetric solutions for system (2.4), we rewrite the model using polar coordinates (ϱ, θ) and impose no dependency of the solution on θ, to obtain:

$$
\begin{aligned}
&\frac{\partial m}{\partial t} = D\frac{1}{\varrho}\frac{\partial}{\partial \varrho}\left[\varrho\frac{\partial m}{\partial \varrho}\right] - \chi\frac{1}{\varrho}\frac{\partial}{\partial \varrho}\left[\varrho\frac{m}{(1+\alpha c)^2}\frac{\partial c}{\partial \varrho}\right] + rmc(1-m),\\
&\frac{\partial c}{\partial t} = \frac{1}{\varrho}\frac{\partial}{\partial \varrho}\left[\varrho\frac{\partial c}{\partial \varrho}\right] + \frac{m}{1+\beta a} - c, \qquad (6.1)\\
&\frac{\partial a}{\partial t} = \frac{1}{\tau}\left\{\frac{1}{\varrho}\frac{\partial}{\partial \varrho}\left[\varrho\frac{\partial a}{\partial \varrho}\right] + \frac{m}{1+\beta a} - a\right\}.
\end{aligned}
$$

We enforce no-flux boundary conditions on the disk $\varrho \in [0,\ R]$, with $R = \beta_{1,n}$, where $\beta_{1,n}$ is the n-th zero of the Bessel function $J_1(\varrho)$, and perform a weakly nonlinear analysis near the bifurcation value, following the same technique used in Section 4. Due to the loss of translation symmetry, we now expect a transcritical instead of a pitchfork bifurcation to occur at criticality. We set $\varepsilon = (\chi - \chi_c)/\chi_c$, define the characteristic time $T = \varepsilon t$, and write the solution of (6.1) close to the homogeneous steady state P^* as the following expansion:

$$
\mathbf{w} = \begin{pmatrix} m - m_0 \\ c - c_0 \\ a - a_0 \end{pmatrix} = \varepsilon \mathbf{w}_1 + \varepsilon^2 \mathbf{w}_2 + \varepsilon^3 \mathbf{w}_3 + O(\varepsilon^4). \qquad (6.2)
$$

Collecting the terms at each order in ε, we obtain a sequence of equations for the $\mathbf{w}_i$s. At $O(\varepsilon)$ we get the following linear problem:

$$
\mathcal{L}^{\chi_c}\mathbf{w}_1 = 0, \qquad (6.3)
$$

where $\mathcal{L}^{\chi_c} = \mathcal{D}^{\chi_c}\frac{1}{\varrho}\frac{\partial}{\partial \varrho}\left[\varrho\frac{\partial}{\partial \varrho}\right] + \mathcal{K}$ and the expressions of $\mathcal{D}$ and $\mathcal{K}$ are given in (3.1). The solution of Eq. (6.3) satisfying the boundary conditions is:

$$
\mathbf{w}_1 = A(T)\boldsymbol{\eta}\, J_0(k_c x), \qquad \text{with } \boldsymbol{\eta} \in Ker(\mathcal{K} - k_c^2\mathcal{D}^{\chi_c}), \qquad (6.4)
$$

where $A(T)$ is the amplitude of the pattern, unknown at this level, and the vector $\boldsymbol{\eta}$ is given by (SM2.2). At $O(\varepsilon^2)$, we obtain the following linear equation:

$$
\mathcal{L}^{\chi_c}\mathbf{w}_2 = \mathbf{F}. \qquad (6.5)
$$

The explicit expression of $\mathbf{F}$ is given in section SM3. Imposing the solvability condition for equation (6.5), we obtain the following evolution equation for the leading order amplitude $A(T)$:

$$
\frac{dA}{dT} = \sigma A - LA^2, \qquad (6.6)
$$

where the explicit expressions of coefficients σ and L (the Landau constant) in terms of the parameters of the full system are computed in section SM3.

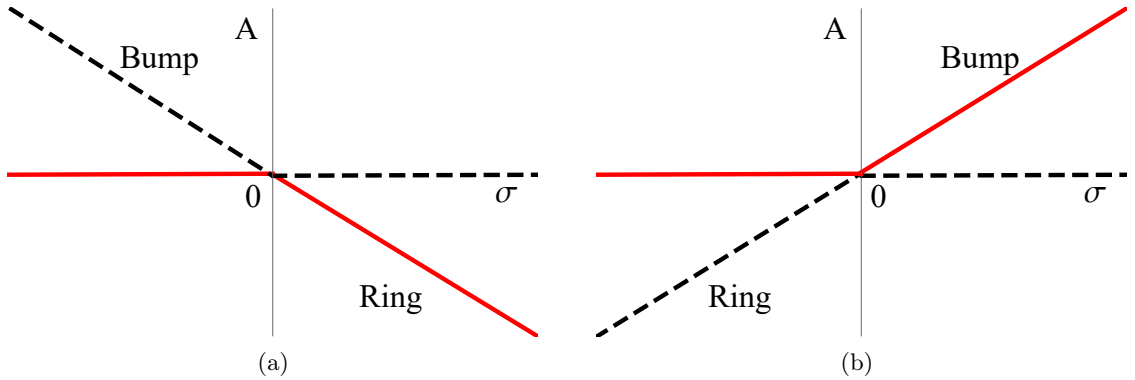

Figure 10: Bifurcation diagram of the transcritical transition of the steady states of (6.6). Solid red (dashed black) lines represent stable (unstable) branches of equilibria. Two qualitatively different plots are possible, depending on being $L < 0$ (shown in (a)), or $L > 0$ (shown in (b))

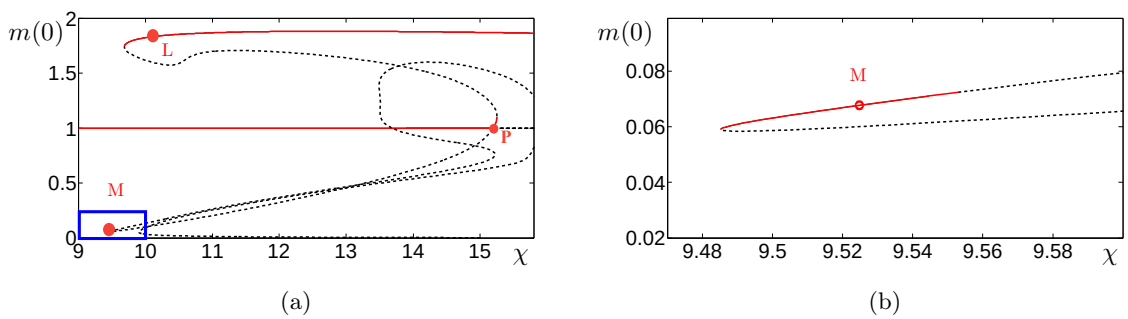

Figure 11: (a): Numerically computed bifurcation diagram of system (6.1) as χ is varied. All the other parameters are fixed as $D = 0.9, \alpha = 1, \beta = 0.1, r = 1, \tau = 30$. Solid red (dashed black) lines represent stable (unstable) branches of equilibria. (b): Enlargement of the box in (a), showing a subcritical stable branch of ring solutions. The stationary solutions corresponding to the points labeled by L and M are shown in Figure 12.

The steady state solutions of Equation (6.6) are $A_1^* = 0$ and $A_2^* = \sigma/L$. The sign of the nontrivial state A_2^* determines qualitatively different solutions: when A_2^* is positive, the solution exhibits a bump at the origin, that we shall call a bump solution. Instead, A_2^* negative corresponds to a solution that has a local minimum at $r = 0$ and a ring at the outer edge of the domain: we shall name it a ring solution. The stability of both types of solutions depends on the sign of L, that determines a transcritical transition of the equilibria of Equation (6.6) at the bifurcation value: for $L < 0$, the steady-state bump solution exists only for negative σ where it is unstable, while the steady-state ring solution exists and is stable for positive values of σ; the converse happens for $L > 0$, see Figure 10.

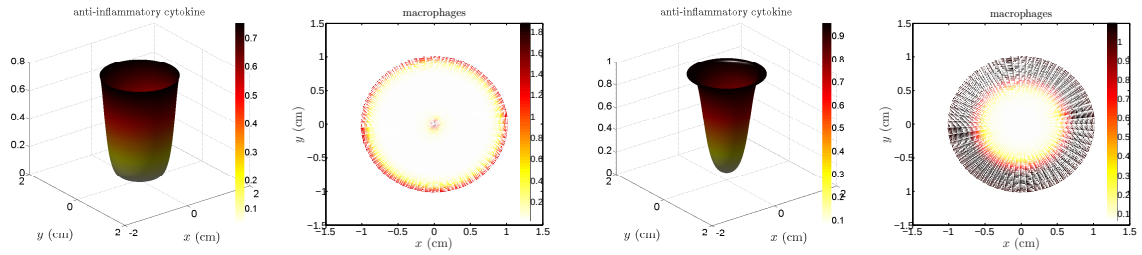

(a) (b) (c) (d)

Figure 12: Stationary solutions of (6.1) corresponding to the points labeled by L and M in Figure 11. The parameters are the same as in Figure 11. (a)-(b): Spatial distribution of the cytokine and of the macrophage density at the point L showing a bull's eye pattern. (c)-(d): Spatial distribution of the cytokine and of the macrophage density at the point M showing a ring solution with a clearer core

We now show some numerical simulations. In all the numerical experiments reported in the present and the next section, we shall fix the values of all the parameters but α and r. We observe that, for r fixed, the Landau constant L is a decreasing function of α, so that negative values of L are easily obtained considering high values of the receptor-binding constant α. Fixing the parameter values as in Figure 11 on the domain $[0,\ \beta_{1,3}]$, where $\beta_{1,3}$ is the 3rd root of the Bessel function J_1, one gets a positive value of the coefficient L in (6.6). Therefore, based on the weakly nonlinear analysis, and close to the transition point, we expect an unstable ring solution below the critical value of χ, (here $\chi_c = 15.2$), and a stable bump solution above the threshold. This result is confirmed by the numerical bifurcation diagram of the full system (6.1), computed through the software AUTO and showed in Figure 11: close to the bifurcation point, the behavior is in fact as predicted by the weakly nonlinear approximation. However, the numerical analysis far from threshold, reveals the existence of two subcritical branches of steady solutions, bistable with the spatially homogeneous state, and corresponding to a bump and a ring solution, respectively. The spatial distribution of the macrophages and cytokine densities at the points labeled by L and M in the bifurcation diagram Figure 11 are shown in Figure 12.

Fixing now the parameters values as in Figure 13 on the spatial domain $[0,\ \beta_{1,15}]$, the weakly nonlinear analysis prescribes a negative value of the coefficient L in (6.6). Therefore we expect an unstable bump solution below the critical value of χ (here $\chi_c = 1.53$) and a ring solution above the threshold. This is in agreement with the numerical bifurcation diagram of (6.1) reported in Figure 13, that, close to the primary bifurcation point, shows a stable branch of ring solutions bifurcating supercritically from the uniform steady state. Far from the primary transition, the numerical analysis detects several bifurcation points (of saddle-node type), from which stable branches of multirings and bull's eye solutions emerge that coexist for large intervals of the chemotaxis coefficient. The spatial distribution of the species densities corresponding to the labeled points in Figure 13 are shown in Figure 14. We notice

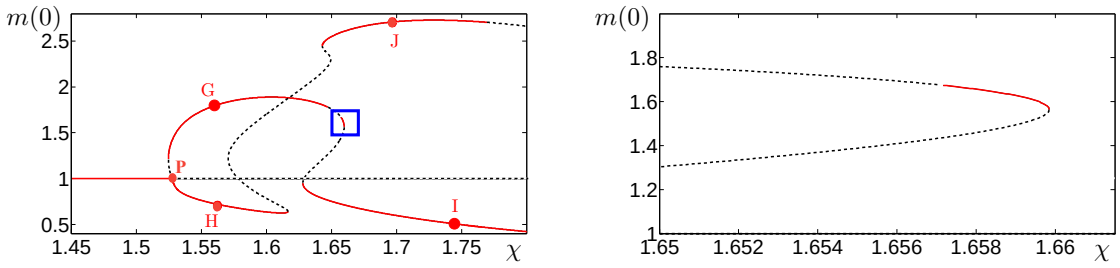

(a) (b)

Figure 13: (a): Numerically computed bifurcation diagram of system (6.1) as χ is varied. The parameters are fixed as $D = 0.9, \alpha = 0.1, \beta = 0.1, r = 0.01, \tau = 30$. Solid red (dashed black) lines represent stable (unstable) branches of equilibria. (b): Enlargement of the box in (a), showing a far-from-equilibrium stable branch of stationary bump solutions arising out of a saddle-node bifurcation. The stationary solutions corresponding to the points labeled by G, H, I and J are shown in Figure 14.

that the points G and J correspond to branches of solutions having a bump at the origin, while H and I correspond to solutions with a local minimum density at $\rho = 0$.

The comparison of the inflammatory patterns showed in Figures 12-14 with the images taken from patients suffering EAC and reported in Figure 15, proves that the proposed model is able to reproduce qualitatively different inflammatory rashes, ranging from one-ring to bull's eye and multi-rings.

7. Numerical simulations in 2D. In the previous section we have mathematically classified stationary solutions of the model (6.1) with circular symmetry. In this section we shall perform a numerical investigation of the full system (2.1)-(2.2) on a 2D square domain. Our goal is two-fold: on the one hand, we want to simulate the evolution in time of the inflammation and compare it with the available medical data, also exploring the effect of varying the numerical values of the parameters. We do not intend to explore all biologically significant regions of the parameter space but show that the system can reproduce phenomena observed in clinical practice. We shall see that the model supports the appearance of localized inflammatory structures having the form of hotspots, bull's eye, and rings, typical of some classes of skin erythemas, such as the EAC. On the other hand, we want to provide a numerical justification to the study performed in the previous Section, showing that an initially highly localized stimulus initiates the formation of inflammatory structures that exhibit radial symmetry.

The numerical solution is computed as described in Section 5. We shall assume that the inflammation is triggered by a highly localized concentration of activated macrophages, deriving from an initial insult. Therefore, as the initial condition, we shall set a bump in the macrophages spatial distribution and zero initial density for both the cytokine species. We enforce Neumann boundary conditions on the square domain $[0, 6]$ cm $\times$ $[0, 6]$ cm.

Figure 16 shows the spatio-temporal evolution of the macrophages in a case when the

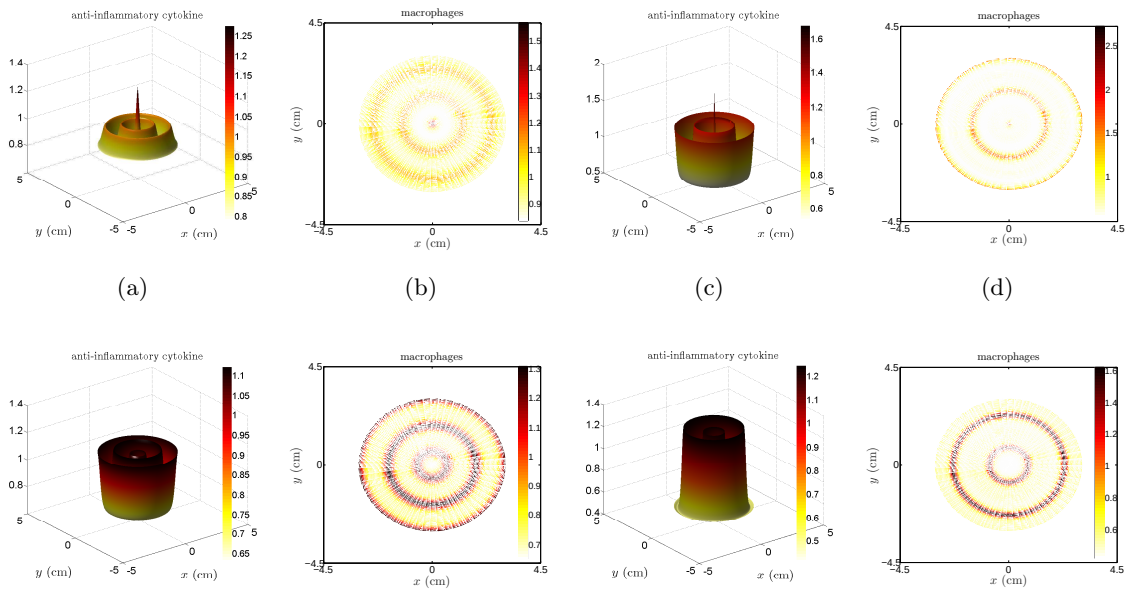

(a) (b) (c) (d)

(e) (f) (g) (h)

Figure 14: Stationary solutions of (6.1) corresponding to the labeled points in Figure 13. The parameters are the same as in Figure 13. Spatial distribution of the cytokine and of the macrophage density (a)-(b): at the point G. (c)-(d): at the point J. (e)-(f): at the point H. (g)-(h): at the point I

(a) (b)

Figure 15: Clinical images of Erythema Annulare Centrifugum. (a): Coexistence of one-ring and bull's eye inflammatory patterns. (b): A polycyclic lesion

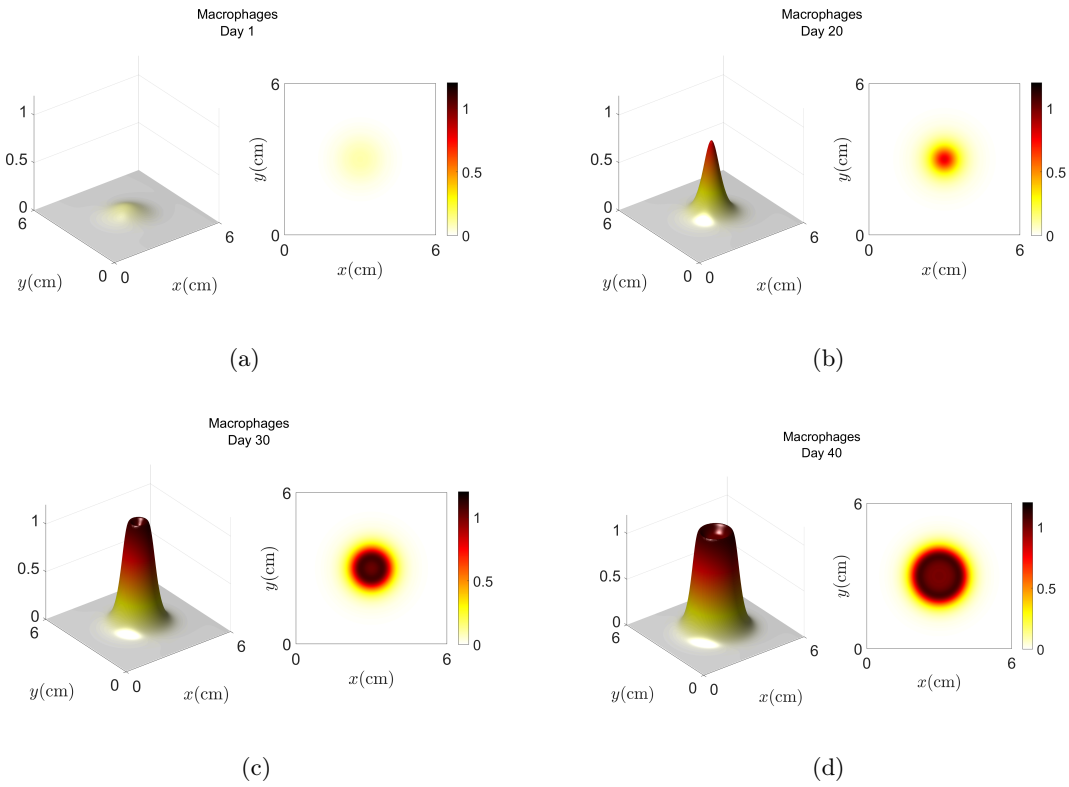

(a) (b) (c) (d)

Figure 16: Temporal evolution of the macrophage species for system (2.4). The parameters are $D = 0.9, \alpha = 0.1, \beta = 0.1, r = 0.1, \tau = 30, \chi = 3$ so that $\chi_c = 4.92$.

chosen value of the parameter χ is below the Turing threshold, so that we expect the formation of a uniformly distributed inflammatory activity. The numerical solution in fact appears as a small red spot (Figure 16b), which subsequently enlarges (Figure 16c, Figure 16d). The proposed model therefore supports the formation of a homogeneous rash.

Figure 17 shows the simulation obtained by increasing the value of χ and keeping the other parameters fixed as before. In this case, initially, the solution appears as a small red spot (Figure 17b), which subsequently enlarges while the central area is clearing (Figures 17c and 17d). The resulting pattern is a ring, which adequately reproduces the evolutive phases of EAC reported in Figure 18. From the numerical simulations, we have also been able to measure the rash growth rate: it is higher in the first days, due to the low density of the anti-inflammatory cytokine, subsequently slowing down until it reaches vanishingly small values. The estimated average growth rate of the diameter turns out to be about 3 mm/day, that is perfectly in agreement with the clinical data [71].

Figure 19 shows a temporal sequence of the numerical solution obtained still increasing the value of χ, while maintaining the others constant. As before, the rash appears on the skin as a little spot (Figure 19b), its diameter increases while the density of macrophages in the

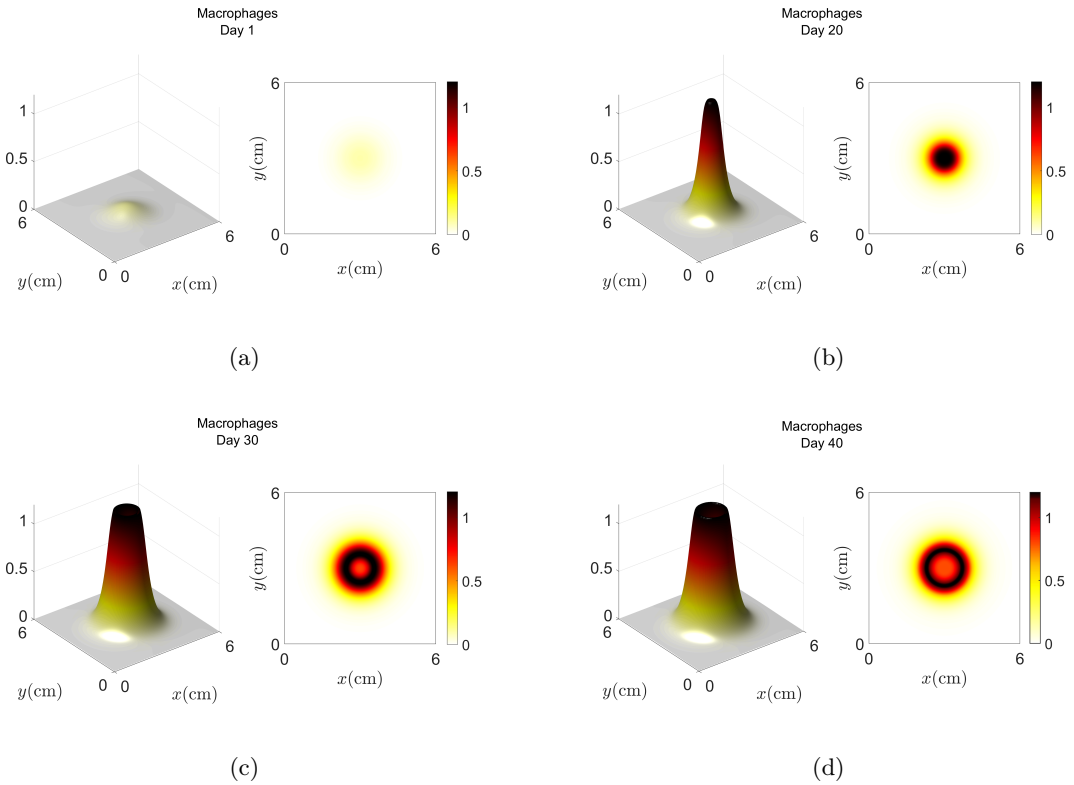

(a) (b)

(c) (d)

Figure 17: Temporal evolution of the macrophage species for system (2.4). The parameters are the same as in Figure 16, except for $\chi = 4.5$.

(a)

Figure 18: Progression of Erythema Annulare Centrifugum in the same patient: it is possible to observe the evolution of the rash, which first appears as a small red-spot, which enlarges as the central area clears. Images are provided by courtesy of RegionalDerm.com

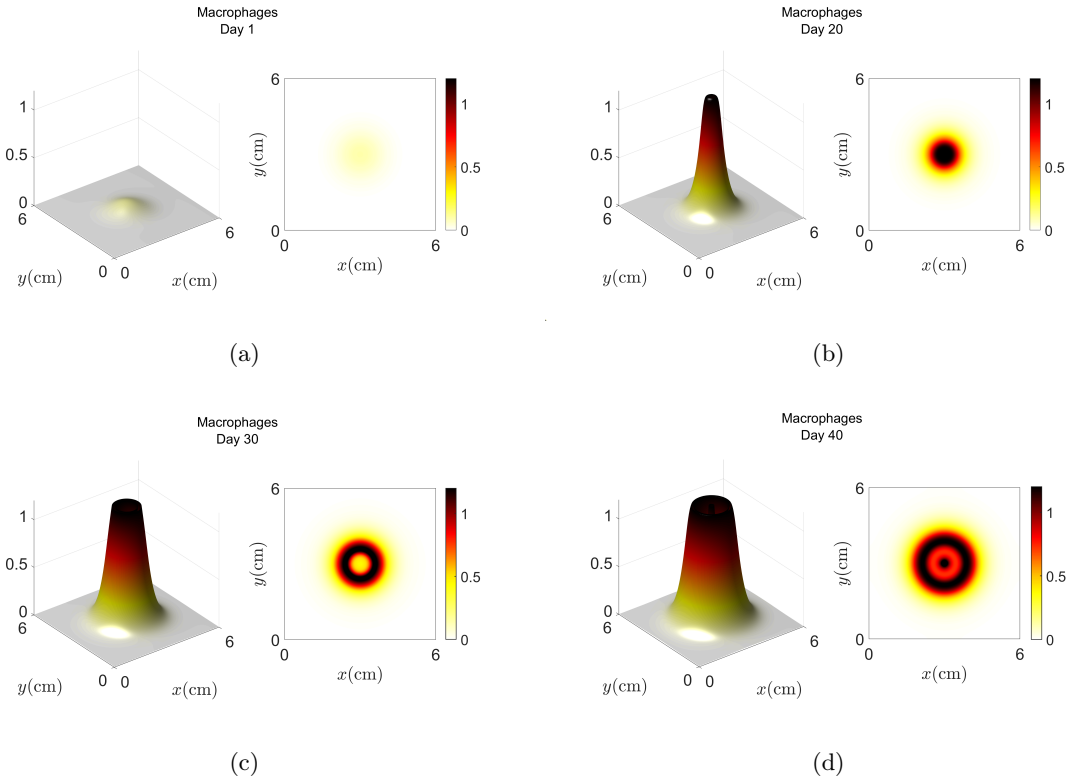

Figure 19: Temporal evolution of the macrophage species for system (2.4). The parameters are as in Figure 16 except for $\chi = 5$

central area decreases (Figure 19c). As time progresses, the macrophage density raises again in the core, so that the resulting solution is a bull's eye pattern (Figure 19d). The effect of increasing the chemotactic parameter with respect to the parameter set given in Figure 17 is that in this case, the erythema growth rate attains a smaller value, namely about 2 mm/day, a value that is still compatible with the medical measurements.

We notice that the above-exposed results are in agreement with the nonlinear analysis performed on the corresponding radial system (6.1) presented in Section 6. In fact, fixing the parameters as in Figure 16, one gets $\chi_c = 4.92$ and a positive value of the the coefficient L appearing in the amplitude equation (6.6). This implies the existence of a ring solution below the Turing threshold and of a bump solution above criticality. On the other hand, far below the Turing threshold, the analysis predicts a homogeneous pattern. Hence all the simulations represented in Figures 16-19 confirm the previsions.

We conclude this section by considering the effect of increasing the activation rate r of macrophages. For the parameter set chosen in Figure 20 the theoretical predictions of the weakly nonlinear analysis prescribe $\chi_c = 9.1$ and $L < 0$, so that a stable branch of stationary rings is expected above the threshold. The resulting simulation of the full system, in fact, shows

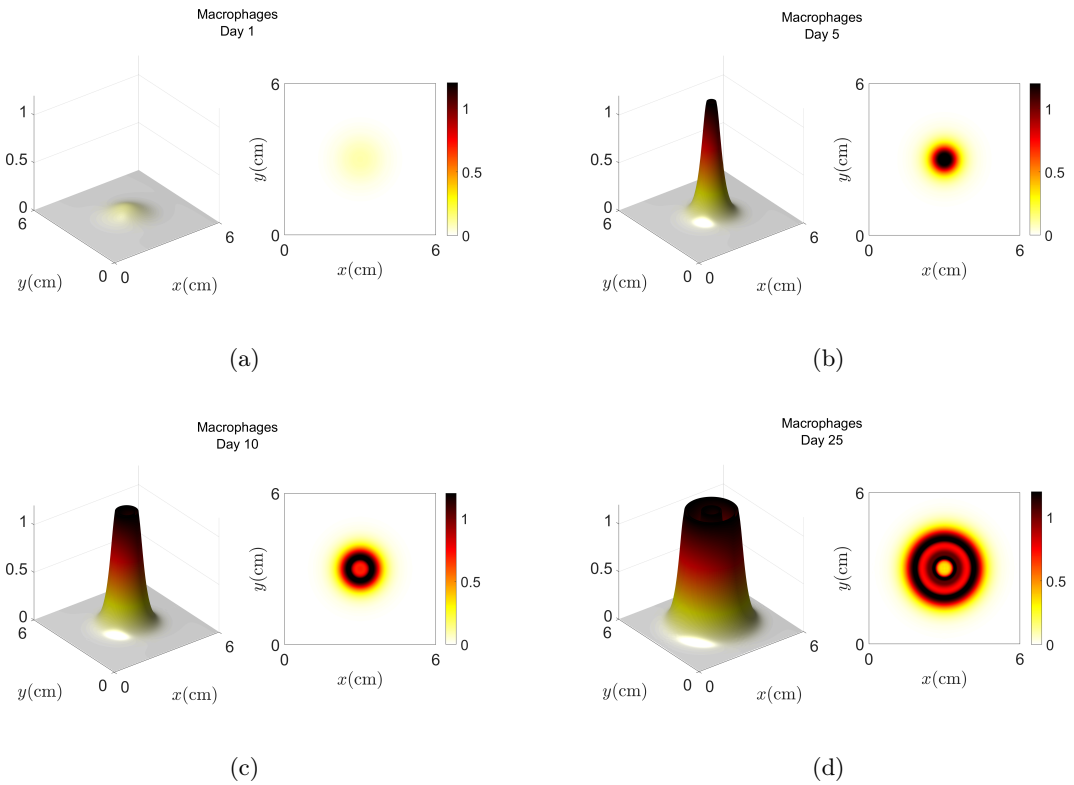

Figure 20: Temporal evolution of the macrophage species for system (2.4). The parameters are: $D = 0.9, \alpha = 0.1, \beta = 0.1, r = 3, \tau = 30, \chi = 10$.

the appearance of two rings around a cleared central area, as shown in Figure 20. Therefore a high value of r not only accelerates the formation of the rash on the skin, but also promotes the formation of more rings.

8. Conclusions. In this paper, we have proposed and investigated a reaction-diffusion-chemotaxis model for acute inflammation. We have performed a theoretical and numerical investigation of the model using realistic values of the parameters, retrieving them in the experimental literature, see Table 1. We have shown that our model can reproduce typical patterns observed in the clinical practice, such as bull's eye and rings, see Figures 15 and 18. Moreover, the model describes the recurrent inflammatory attacks reported by patients suffering from REM. This is the first time a mathematical model can reproduce these clinical patterns to the best of our knowledge. The solutions mentioned above are the result of a Turing or a wave bifurcation destabilizing a uniform equilibrium. We have constructed these solutions using the amplitude equation analysis and validated them by detailed numerical simulations of the complete system. Through a numerical bifurcation analysis far from the instability threshold, we have also found that the inclusion of a macrophage activation term is responsible for generating chaos. The presence in this model of sequences of bifurcations

leading to complex spatio-temporal dynamics can be considered a hallmark of self-organized criticality in macrophages dynamics [60]: the immune system might benefit from operating in the proximity of a critical boundary between organized and disorganized states, maintaining the right balance between stability and adaptability. We believe that the wide variety of patterns supported by the two systems presented in this paper and [66] gives evidence that this class of models captures the main mechanisms driving inflammatory rashes.

We point out several open problems left unsolved by the present analysis and possible directions for future research. First, one should investigate the formation of localized structures, like those organized in a homoclinic snaking bifurcation scenario, that could account for the appearance of isolated foci of inflammation. Second, we believe that the investigation of the mechanisms underlying the appearance of spatio-temporal irregular solutions requires further study. In fact, the oscillations of the periodic structures reported in the numerical simulations of Figures 7 and 9 are unexpected based on the linear analysis since, in the considered parameter regime, the proposed system does not support any Hopf or wave instability. We conjecture that a spatial resonance of the fundamental Turing mode with its subharmonics originates the observed spatio-temporal periodic solutions, analogously to what is discussed in [28]. It would be interesting to derive the normal forms of the resonant interaction and investigate the phase instabilities which initiate the chaotic dynamics [11]. From the modeling point of view, we remark that this model does not describe phenomena occurring in later stages of the inflammatory process, like sepsis or spontaneous resolution. A refined model would be necessary to follow the inflammatory process in these phases. Finally, since a broad class of anti-inflammatory drugs acts on macrophages' activation rate, we believe that the present system could be a useful tool to design optimized therapies.

Acknowledgments. The authors acknowledge the financial support of GNFM-INdAM and the Italian MIUR through project PRIN2017 "Multiscale phenomena in Continuum Mechanics: singular limits, off-equilibrium and transitions" (project number: 2017YBKNCE).

The authors thank two anonymous referees for several comments and suggestions that significantly helped improve the paper's presentation.

REFERENCES

[1] J. Abrams, C. Figdor, R. De Waal Malefyt, B. Bennett, and J. De Vries, *Interleukin 10(IL-10) inhibits cytokine synthesis by human monocytes: An autoregulatory role of IL-10 produced by monocytes*, Journal of Experimental Medicine, 174 (1991), pp. 1209–1220.

[2] J. Ahn, *Global well-posedness and asymptotic stabilization for chemotaxis system with signal-dependent sensitivity*, Journal of Differential Equations, 266 (2019), pp. 6866–6904.

[3] A. Anma, K. Sakamoto, and T. Yoneda, *Unstable subsystems cause Turing instability*, Kodai Mathematical Journal, 35 (2012), pp. 215–247.

[4] P. Bak, C. Tang, and K. Wiesenfeld, *Self-organized criticality: An explanation of the* $1/f$ *noise*, Physical Review Letters, 59 (1987), pp. 381–384.

[5] M. Barnett, K. Lamb, K. Costello, and M. Pike, *Characterization of Interleukin-8 receptors in human neutrophil membranes: Regulation by guanine nucleotides*, BBA - Molecular Cell Research, 1177 (1993), pp. 275–282.

[6] M. Beekman, D. Sumpter, and F. Ratnieks, *Phase transition between disordered and ordered foraging in pharaoh's ants*, Proceedings of the National Academy of Sciences of the United States of America, 98 (2001), pp. 9703–9706.

[7] J. Beggs and D. Plenz, *Neuronal avalanches in neocortical circuits*, Journal of Neuroscience, 23 (2003), pp. 11167–11177.

[8] E. Bilotta, F. Gargano, V. Giunta, M. C. Lombardo, P. Pantano, and M. Sammartino, *Eckhaus and zigzag instability in a chemotaxis model of multiple sclerosis*, Atti della Accademia Peloritana dei Pericolanti-Classe di Scienze Fisiche, Matematiche e Naturali, 96 (2018), p. 9.

[9] B. Burke and C. E. Lewis, *The Macrophage*, Oxford University Press, 2nd ed., 2002.

[10] E. Cammarota, C. Soriani, R. Taub, F. Morgan, J. Sakai, S. Veatch, C. Bryant, and P. Cicuta, *Criticality of plasma membrane lipids reflects activation state of macrophage cells*, Journal of the Royal Society Interface, 17 (2020).

[11] M. Cheng and H.-C. Chang, *Subharmonic instabilities of finite-amplitude monochromatic waves*, Physics of Fluids A: Fluid Dynamics, 4 (1992), pp. 505–523.

[12] V. Chitu, Y.-G. Yeung, W. Yu, S. Nandi, and E. Stanley, *Measurement of macrophage growth and differentiation*, Current Protocols in Immunology, (2011).

[13] G. Consolo, C. Curro, and G. Valenti, *Supercritical and subcritical Turing pattern formation in a hyperbolic vegetation model for flat arid environments*, Physica D: Nonlinear Phenomena, 398 (2019), pp. 141–163.

[14] G. Cross, *Three types of matrix stability*, Linear Algebra and Its Applications, 20 (1978), pp. 253–263.

[15] J. Daley, S. Brancato, A. Thomay, J. Reichner, and J. Albina, *The phenotype of murine wound macrophages*, Journal of Leukocyte Biology, 87 (2010), pp. 59–67.

[16] J. Darier, *De l'érythème annulaire centrifuge (érythème papulo-circiné migrateur et chronique) et de quelques éruptions analogues*, Annales de dermatologie et de syphiligraphie, 6 (1916), pp. 57–76.

[17] L. Davies, S. Jenkins, J. Allen, and P. Taylor, *Tissue-resident macrophages*, Nature Immunology, 14 (2013), pp. 986–995.

[18] B. Delavary, W. van der Veer, M. van Egmond, F. Niessen, and R. Beelen, *Macrophages in skin injury and repair*, Immunobiology, 216 (2011), pp. 753–762.

[19] L. Desvillettes and V. Giunta, *Existence and regularity for a chemotaxis model involved in the modeling of multiple sclerosis*, Ricerche di Matematica, (2020).

[20] J. Dunster, *The macrophage and its role in inflammation and tissue repair: Mathematical and systems biology approaches*, Wiley Interdisciplinary Reviews: Systems Biology and Medicine, 8 (2016), pp. 87–99.

[21] S. Ei, H. Izuhara, and M. Mimura, *Spatio-temporal oscillations in the Keller-Segel system with logistic growth*, Physica D: Nonlinear Phenomena, 277 (2014), pp. 1–21.

[22] B. Erickson, K. Sperber, and W. Frishman, *Toll-like receptors: New therapeutic targets for the treatment of atherosclerosis, acute coronary syndromes, and myocardial failure*, Cardiology in Review, 16 (2008), pp. 273–279.

[23] K.-H. Farh, A. Marson, J. Zhu, M. Kleinewietfeld, W. Housley, S. Beik, N. Shoresh, H. Whitton, R. Ryan, A. Shishkin, M. Hatan, M. Carrasco-Alfonso, D. Mayer, C. Luckey, N. Patsopoulos, P. De Jager, V. Kuchroo, C. Epstein, M. Daly, D. Hafler, and B. Bernstein, *Genetic and epigenetic fine mapping of causal autoimmune disease variants*, Nature, 518 (2015), pp. 337–343.

[24] B. Farrell, R. Daniele, and D. Lauffenburger, *Quantitative relationships between single-cell and cell-population model parameters for chemosensory migration responses of alveolar macrophages to C5a*, Cell Motility and the Cytoskeleton, 16 (1990), pp. 279–293.

[25] G. Gambino, M. Lombardo, and M. Sammartino, *A velocity-diffusion method for a Lotka-Volterra system with nonlinear cross and self-diffusion*, Applied Numerical Mathematics, 59 (2009), pp. 1059–1074.

[26] G. Gambino, M. Lombardo, and M. Sammartino, *Turing instability and traveling fronts for a nonlinear reaction-diffusion system with cross-diffusion*, Mathematics and Computers in Simulation, 82 (2012), pp. 1112–1132.

[27] G. Gambino, M. Lombardo, and M. Sammartino, *Pattern formation driven by cross-diffusion in a 2D domain*, Nonlinear Analysis: Real World Applications, 14 (2013), pp. 1755–1779.

[28] G. Gambino, M. Lombardo, and M. Sammartino, *Cross-diffusion-induced subharmonic spatial resonances in a predator-prey system*, Physical Review E - Statistical, Nonlinear, and Soft Matter Physics, 97 (2018).

[29] G. Gambino, M. Lombardo, M. Sammartino, and V. Sciacca, *Turing pattern formation in the Brusselator system with nonlinear diffusion*, Physical Review E - Statistical, Nonlinear, and Soft Matter Physics, 88 (2013).
[30] D. Gammack, C. Doering, and D. Kirschner, *Macrophage response to mycobacterium tuberculosis infection*, Journal of Mathematical Biology, 48 (2004), pp. 218–242.
[31] G. Goodhill, *Diffusion in axon guidance*, European Journal of Neuroscience, 9 (1997), pp. 1414–1421.
[32] Q. Hamid and M. Tulic, *Immunobiology of asthma*, Annual Review of Physiology, 71 (2009), pp. 489–507.
[33] S. Hata, H. Nakao, and A. Mikhailov, *Sufficient conditions for wave instability in three-component reaction-diffusion systems*, Progress of Theoretical and Experimental Physics, 2014 (2014).
[34] T. Hillen and K. Painter, *A user's guide to PDE models for chemotaxis*, Journal of Mathematical Biology, 58 (2009), pp. 183–217.
[35] J. Hobbs, J. Smith, and J. Beggs, *Aberrant neuronal avalanches in cortical tissue removed from juvenile epilepsy patients*, Journal of Clinical Neurophysiology, 27 (2010), pp. 380–386.
[36] D. Horstmann and G. Wang, *Blow-up in a chemotaxis model without symmetry assumptions*, European Journal of Applied Mathematics, 12 (2001), pp. 159–177.
[37] A. Hudspeth, F. Jülicher, and P. Martin, *A critique of the critical cochlea: Hopf - a bifurcation - is better than none*, Journal of Neurophysiology, 104 (2010), pp. 1219–1229.
[38] M. Hyman, L. A. Segel, A. S. Perelson, and S. N. Klaus, *Rash theory*, in Theoretical and Experimental Insights into Immunology, NATO ASI Series, A. S. Perelson and G. Weisbuch, eds., Springer-Verlag, 1992, pp. 333–352.
[39] S. Ingen-Housz-Oro, N. Ortonne, and O. Chosidow, *The diagnosis is in the rings*, BMJ (Online), 359 (2017).
[40] H. Jaeschke and C. Smith, *Mechanisms of neutrophil-induced parenchymal cell injury*, Journal of Leukocyte Biology, 61 (1997), pp. 647–653.
[41] T. Kolokolnikov, J. Wei, and A. Alcolado, *Basic mechanisms driving complex spike dynamics in a chemotaxis model with logistic growth*, SIAM Journal on Applied Mathematics, 74 (2014), pp. 1375–1396.
[42] P. Krzyszczyk, R. Schloss, A. Palmer, and F. Berthiaume, *The role of macrophages in acute and chronic wound healing and interventions to promote pro-wound healing phenotypes*, Frontiers in Physiology, 9 (2018).
[43] R. Kumar, G. Clermont, Y. Vodovotz, and C. Chow, *The dynamics of acute inflammation*, Journal of Theoretical Biology, 230 (2004), pp. 145–155.
[44] D. Laskin, V. Sunil, C. Gardner, and J. Laskin, *Macrophages and tissue injury: Agents of defense or destruction?*, Annual Review of Pharmacology and Toxicology, 51 (2011), pp. 267–288.
[45] K. Law, M. Weiden, T. Harkin, K. Tchou-Wong, C. Chi, and W. Rom, *Increased release of interleukin-1β, interleukin-6, and tumor necrosis factor-α by bronchoalveolar cells lavaged from involved sites in pulmonary tuberculosis*, American Journal of Respiratory and Critical Care Medicine, 153 (1996), pp. 799–804.
[46] T. Lawrence and D. Gilroy, *Chronic inflammation: A failure of resolution?*, International Journal of Experimental Pathology, 88 (2007), pp. 85–94.
[47] S. C. Lee, W. Liu, D. W. Dickson, C. F. Brosnan, and J. W. Berman, *Cytokine production by human fetal microglia and astrocytes. Differential induction by lipopolysaccharide and IL-1-beta.*, The Journal of Immunology, 150 (1993), pp. 2659–2667.
[48] M. Lerch, C. Mainetti, B. Terziroli Beretta-Piccoli, and T. Harr, *Current perspectives on erythema multiforme*, Clinical Reviews in Allergy and Immunology, 54 (2018), pp. 177–184.
[49] M. Luca, A. Chavez-Ross, L. Edelstein-Keshet, and A. Mogilner, *Chemotactic signaling, microglia, and Alzheimer's disease senile plaques: Is there a connection?*, Bulletin of Mathematical Biology, 65 (2003), pp. 693–730.
[50] M. Ma, C. Ou, and Z.-A. Wang, *Stationary solutions of a volume-filling chemotaxis model with logistic growth and their stability*, SIAM Journal on Applied Mathematics, 72 (2012), pp. 740–766.
[51] M. Ma and Z.-A. Wang, *Global bifurcation and stability of steady states for a reaction-diffusion-chemotaxis model with volume-filling effect*, Nonlinearity, 28 (2015), p. 2639.
[52] A. Mantovani, S. Sozzani, M. Locati, P. Allavena, and A. Sica, *Macrophage polarization:*

Tumor-associated macrophages as a paradigm for polarized M2 mononuclear phagocytes, Trends in Immunology, 23 (2002), pp. 549–555.

[53] P. Martin and S. Leibovich, *Inflammatory cells during wound repair: The good, the bad and the ugly*, Trends in Cell Biology, 15 (2005), pp. 599–607.

[54] T. Mora and W. Bialek, *Are biological systems poised at criticality?*, Journal of Statistical Physics, 144 (2011), pp. 268–302.

[55] J. D. Murray, *Mathematical Biology II. Spatial Models and Biomedical Applications*, Interdisciplinary Applied Mathematics, Springer-Verlag New York, 3 ed., 2003.

[56] M. Muñoz, *Colloquium: Criticality and dynamical scaling in living systems*, Reviews of Modern Physics, 90 (2018).

[57] S. Nagaraja, A. Wallqvist, J. Reifman, and A. Mitrophanov, *Computational approach to characterize causative factors and molecular indicators of chronic wound inflammation*, Journal of Immunology, 192 (2014), pp. 1824–1834.

[58] G. Nicolis and I. Prigogine, *Self-Organization in Nonequilibrium Systems: From Dissipative Structures to Order Through Fluctuations*, Wiley, New York, 1977.

[59] A. Nimmerjahn, F. Kirchhoff, and F. Helmchen, *Neuroscience: Resting microglial cells are highly dynamic surveillants of brain parenchyma in vivo*, Science, 308 (2005), pp. 1314–1318.

[60] M. Nykter, N. Price, M. Aldana, S. Ramsey, S. Kauffman, L. Hood, O. Yli-Harja, and I. Shmulevich, *Gene expression dynamics in the macrophage exhibit criticality*, Proceedings of the National Academy of Sciences of the United States of America, 105 (2008), pp. 1897–1900.

[61] K. Osaki, T. Tsujikawa, A. Yagi, and M. Mimura, *Exponential attractor for a chemotaxis-growth system of equations*, Nonlinear Analysis, Theory, Methods and Applications, 51 (2002), pp. 119–144.

[62] K. Painter, *Mathematical models for chemotaxis and their applications in self-organisation phenomena*, Journal of Theoretical Biology, 481 (2019), pp. 162–182.

[63] K. Painter and T. Hillen, *Volume-filling and quorum-sensing in models for chemosensitive movement*, Canadian Appl. Math. Quart, 10 (2002), pp. 501–543.

[64] K. Painter and T. Hillen, *Spatio-temporal chaos in a chemotaxis model*, Physica D: Nonlinear Phenomena, 240 (2011), pp. 363–375.

[65] F. Paquin-Lefebvre, W. Nagata, and M. Ward, *Pattern formation and oscillatory dynamics in a two-dimensional coupled bulk-surface reaction-diffusion system*, SIAM Journal on Applied Dynamical Systems, 18 (2019), pp. 1334–1390.

[66] K. Penner, B. Ermentrout, and D. Swigon, *Pattern formation in a model of acute inflammation*, SIAM Journal on Applied Dynamical Systems, 11 (2012), pp. 629–660.

[67] J. Pinilla-Ibarz, B. Shah, and J. Dubovsky, *The biological basis for immunotherapy in patients with chronic myelogenous leukemia*, Cancer Control, 16 (2009), pp. 141–152.

[68] C. Procesi, *Lie Groups - An Approach Through Invariants and Representations*, Springer, Universitext, 2006.

[69] I. Ramirez-Zuniga, J. Rubin, D. Swigon, and G. Clermont, *Mathematical modeling of energy consumption in the acute inflammatory response*, Journal of Theoretical Biology, 460 (2019), pp. 101–114.

[70] A. Reynolds, J. Rubin, G. Clermont, J. Day, Y. Vodovotz, and G. Bard Ermentrout, *A reduced mathematical model of the acute inflammatory response: I. derivation of model and analysis of anti-inflammation*, Journal of Theoretical Biology, 242 (2006), pp. 220–236.

[71] A. Rook, D. S. Wilkinson, F. J. B. Ebling, R. H. Champion, and J. L. Burton, *Textbook of Dermatology*, Oxford: Blackwell Scientific Publication., 1991.

[72] J. Sasaki and T. Sasaki, *Regulation of Chronic Inflammation by Control of Macrophage Activation and Polarization*, Springer Japan, Tokyo, 2016, pp. 97–107.

[73] R. Satnoianu, M. Menzinger, and P. Maini, *Turing instabilities in general systems*, Journal of Mathematical Biology, 41 (2000), pp. 493–512.

[74] R. Schaaf, *Stationary solutions of chemotaxis systems*, Transactions of the American Mathematical Society, 292 (1985), pp. 531–556.

[75] J. Schofield, F. Tatnall, and I. Leight, *Recurrent erythema multiforme: Clinical features and treatment in a large series of patients*, British Journal of Dermatology, 128 (1993), pp. 542–545.

[76] S. Shiozawa, *Cause of systemic lupus erythematosus: A novel self-organized criticality theory of autoim-*

munity, Expert Review of Clinical Immunology, 7 (2011), pp. 715–717.
[77] R. Snyderman and E. Fudman, *Demonstration of a chemotactic factor receptor on macrophages*, Journal of Immunology, 124 (1980), pp. 2754–2757.
[78] O. Sokumbi and D. Wetter, *Clinical features, diagnosis, and treatment of erythema multiforme: A review for the practicing dermatologist*, International Journal of Dermatology, 51 (2012), pp. 889–902.
[79] G. Solovey, L. Alonso, T. Yanagawa, N. Fujii, M. Magnasco, G. Cecchi, and A. Proekt, *Loss of consciousness is associated with stabilization of cortical activity*, Journal of Neuroscience, 35 (2015), pp. 10866–10877.
[80] P. Sorrentino, R. Rucco, F. Baselice, R. De Micco, A. Tessitore, A. Hillebrand, L. Mandolesi, M. Breakspear, L. Gollo, and G. Sorrentino, *Flexible brain dynamics underpins complex behaviours as observed in Parkinson's disease*, Scientific Reports, 11 (2021).
[81] R. Stout, *Editorial: Macrophage functional phenotypes: No alternatives in dermal wound healing?*, Journal of Leukocyte Biology, 87 (2010), pp. 19–21.
[82] A. W. Thomson and M. T. Lotze, *The Cytokine Handbook*, Academic Press, London, 2003.
[83] P. Tong, B. Roediger, N. Kolesnikoff, M. Biro, S. Tay, R. Jain, L. Shaw, M. Grimbaldeston, and W. Weninger, *The skin immune atlas: Three-dimensional analysis of cutaneous leukocyte subsets by multiphoton microscopy*, Journal of Investigative Dermatology, 135 (2015), pp. 84–93.
[84] R. Tranquillo, S. Zigmond, and D. Lauffenburger, *Measurement of the chemotaxis coefficient for human neutrophils in the under-agarose migration assay*, Cell Motility and the Cytoskeleton, 11 (1988), pp. 1–15.
[85] P. Travers, M. Walport, M. Schlomchik, and C. A. Janeway, *Immunobiology: the immune system in health and disease*, Taylor & Francis, 5th ed., 2001.
[86] L. Tuckerman and D. Barkley, *Bifurcation analysis of the Eckhaus instability*, Physica D: Nonlinear Phenomena, 46 (1990), pp. 57–86.
[87] N. Valeyev, C. Hundhausen, Y. Umezawa, N. Kotov, G. Williams, A. Clop, C. Ainali, C. Ouzounis, S. Tsoka, and F. Nestle, *A systems model for immune cell interactions unravels the mechanism of inflammation in human skin*, PLoS Computational Biology, 6 (2010).
[88] S. L. Veatch and P. Cicuta, *Critical lipidomics: The consequences of lipid miscibility in biological membranes*, in Physics of Biological Membranes, P. Bassereau and P. Sens, eds., Springer International Publishing, Cham, 2018, pp. 141–168.
[89] Y. Vodovotz, *Deciphering the complexity of acute inflammation using mathematical models*, Immunologic Research, 36 (2006), pp. 237–245.
[90] Y. Vodovotz, G. Clermont, C. Chow, and G. An, *Mathematical models of the acute inflammatory response*, Current Opinion in Critical Care, 10 (2004), pp. 383–390.
[91] Z. Wang and T. Hillen, *Classical solutions and pattern formation for a volume filling chemotaxis model*, Chaos, 17 (2007).
[92] K. Weber-Matthiesen and W. Sterry, *Organization of the monocyte/macrophage system of normal human skin*, Journal of Investigative Dermatology, 95 (1990), pp. 83–89.
[93] D. Wetter and M. Davis, *Recurrent erythema multiforme: Clinical characteristics, etiologic associations, and treatment in a series of 48 patients at Mayo Clinic, 2000 to 2007*, Journal of the American Academy of Dermatology, 62 (2010), pp. 45–53.
[94] J. Wigginton and D. Kirschner, *A model to predict cell-mediated immune regulatory mechanisms during human infection with mycobacterium tuberculosis*, Journal of Immunology, 166 (2001), pp. 1951–1967.
[95] M. Winkler, *Boundedness in the higher-dimensional parabolic-parabolic chemotaxis system with logistic source*, Communications in Partial Differential Equations, 35 (2010), pp. 1516–1537.
[96] M. Winkler, *Finite-time blow-up in the higher-dimensional parabolic-parabolic Keller-Segel system*, Journal des Mathematiques Pures et Appliquees, 100 (2013), pp. 748–767.
[97] D. J. Wollkind, V. Manoranjan, and L. Zhang, *Weakly nonlinear stability analyses of prototype reaction-diffusion model equations*, SIAM Review, 36 (1994), pp. 176–214.